



HAL
open science

Impact of osmotic pressure on the stability of Taylor vortices

Rouae Ben Dhia, Nils Tilton, Denis Martinand

► **To cite this version:**

Rouae Ben Dhia, Nils Tilton, Denis Martinand. Impact of osmotic pressure on the stability of Taylor vortices. *Journal of Fluid Mechanics*, 2022, 933, pp.A51. 10.1017/jfm.2021.1101 . hal-03533753

HAL Id: hal-03533753

<https://hal.science/hal-03533753v1>

Submitted on 19 Jan 2022

HAL is a multi-disciplinary open access archive for the deposit and dissemination of scientific research documents, whether they are published or not. The documents may come from teaching and research institutions in France or abroad, or from public or private research centers.

L'archive ouverte pluridisciplinaire **HAL**, est destinée au dépôt et à la diffusion de documents scientifiques de niveau recherche, publiés ou non, émanant des établissements d'enseignement et de recherche français ou étrangers, des laboratoires publics ou privés.

Impact of osmotic pressure on the stability of Taylor vortices.

Rouae BEN DHIA¹, Nils TILTON² and Denis MARTINAND^{1†}

¹Aix-Marseille Univ, CNRS, Centrale Marseille, M2P2, Marseille, France

²Mechanical Engineering, Colorado School of Mines, Golden, CO 80401 USA

(Received xx; revised xx; accepted xx)

We use linear stability analysis and direct numerical simulations (DNS) to investigate the coupling between centrifugal instabilities, solute transport and osmotic pressure in a Taylor–Couette configuration that models rotating dynamic filtration devices. The geometry consists of a Taylor–Couette cell with a superimposed radial throughflow of solvent across two semi-permeable cylinders. Both cylinders totally reject the solute, inducing the build-up of a concentration boundary layer. The solute retroacts on the velocity field via the osmotic pressure associated with the concentration differences across the semi-permeable cylinders. Our results show that the presence of osmotic pressure strongly alters the dynamics of the centrifugal instabilities and substantially reduces the critical conditions above which Taylor vortices are observed. It is also found that this enhancement of the hydrodynamic instabilities eventually plateaus as the osmotic pressure is further increased. We propose a mechanism to explain how osmosis and instabilities cooperate and develop an analytical criterion to bound the parameter range for which osmosis fosters the hydrodynamic instabilities.

Key words: Authors should not enter keywords on the manuscript, as these must be chosen by the author during the online submission process and will then be added during the typesetting process (see <http://journals.cambridge.org/data/relatedlink/jfm-keywords.pdf> for the full list)

1. Introduction

Reverse osmosis (RO) systems play a key role in the water-energy-climate nexus due to their applications to seawater desalination and the treatment of municipal, agricultural and industrial wastewaters. RO removes solutes from a feed solution by pressurizing the feed and flowing it over a semi-permeable membrane sheet, as sketched in figure 1. The pressure difference across the membrane forces water through the membrane, while solutes are mostly blocked. Though modern RO is usually far more efficient than conventional distillation processes (Ghaffour *et al.* 2013), it remains an energy-intensive process due to the large feed pressures (up to 80 bars) required to overcome the small membrane permeability and the large osmotic pressure difference across the membrane. To date, these energy demands have been primarily reduced by developing new membrane materials and energy recovery devices (Wang *et al.* 2014). Further improvements must address a phenomenon called concentration polarization, which is the accumulation of filtered solutes adjacent to the membrane surface, forming a concentration boundary

† Email address for correspondence: denis.martinand@univ-amu.fr

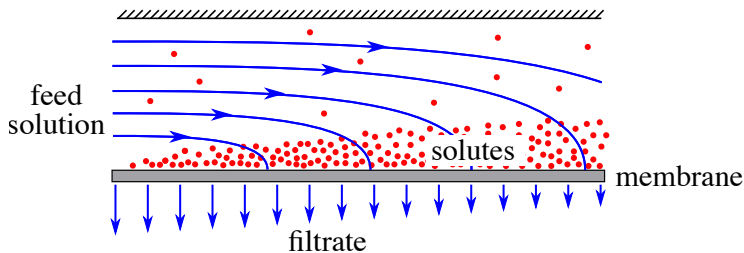


FIGURE 1. Sketch demonstrating concentration polarization in a plate-and-frame reverse osmosis system.

layer, or “polarization layer”, as sketched in figure 1. This accumulation increases the transmembrane osmotic pressure and reduces the fraction of water recovered from the feed (Sablani *et al.* 2001). It also leads to mineral scaling, which is the precipitation of salts onto the membrane surface. Mineral scaling reduces membrane life and increases downtime and maintenance costs (Lyster *et al.* 2009). It also contributes to biofouling by driving nutrients to the membrane surface (Mansouri *et al.* 2010). More broadly, concentration polarization is a challenge in nearly all membrane filtration processes, including ultrafiltration processes, where it leads to the formation of gel layers, and thermally-driven membrane distillation processes (Lou *et al.* 2019, 2020) where it impedes the treatment of high-concentration waste brine.

Current efforts to decrease concentration polarization often focus on the hydrodynamic role of feed spacers (Ahmad & Lau 2006). Feed spacers are a mesh-like material placed in the feed channel to support fragile membrane sheets and provide room for feed flow tangential to the membrane. For sufficiently large feed flow rates, the filaments of these spacers also generate unsteady vortical flow structures due to a wake instability similar to the von Kármán vortex street. Experimental and numerical works suggest that these vortical structures increase the transmembrane flow by stirring and attenuating concentration boundary layers (refer to the works of Haidari *et al.* 2016, 2018*a,b*, for reviews). Despite the considerable work to date, spacers are still primarily designed using experience and trial-and-error. Due to their complicated geometry, our knowledge of the flow regime in RO systems with feed spacers remains inadequate. Meanwhile, the more fundamental question of how vortical structures might interact with concentration polarization is itself poorly understood.

The present study investigates an aspect of this latter question by considering RO in the Taylor-Couette cell sketched in figure 2(*a*). In the annular gap between two concentric cylinders, a feed solution composed of a solvent and a solute is set in motion by the rotation of the inner cylinder. There is no applied pressure gradient in the axial direction, and contrary to traditional RO systems, there is no mean axial flow. Both cylinders are semi-permeable membranes through which solvent can flow, while the solute is retained in the annular gap. The inner membrane surrounds a cavity filled with pure solvent maintained at a desired constant pressure P_{in} . The region outside the outer membrane is similarly filled with solvent maintained at the constant pressure P_{out} . Note that figure 2(*a*) only shows the fluid in the annular gap. Applying a radial pressure difference $\Delta P = P_{\text{in}} - P_{\text{out}}$ drives a radial throughflow of solvent across both cylindrical membranes and the gap. The solute advected by the radial throughflow forms a concentration boundary layer at the cylinder through which the solvent exits the gap.

We show that below a critical rotation rate of the inner cylinder, the flow fields in

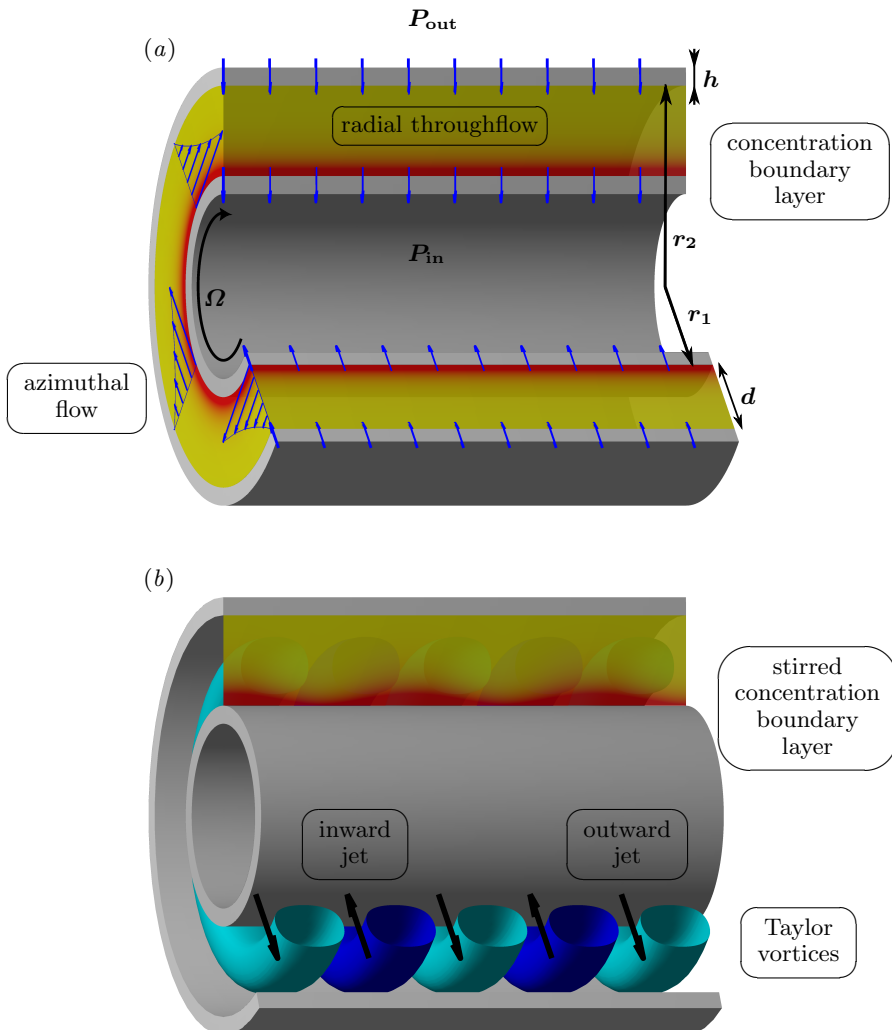


FIGURE 2. (a): Sketch of the base-state flow and concentration field in a Taylor-Couette cell with two semi-permeable cylinders and a superimposed radial inflow. (b) Sketch of the counter-rotating Taylor vortices (the blue online toroidal streamtubes), the outward and inward jets of which (the black arrows) advect the concentration boundary layer to form zones of alternate accumulation and depletion of solute, shown in the planform above.

this set-up admit a simple steady analytical solution, as shown in figure 2(a). Beyond that rotation rate, toroidal Taylor vortices appear as sketched in figure 2(b). These counter-rotating vortices form alternating outward and inward radial jets. These jets stir the concentration boundary layer and form alternating regions of solute accumulation and depletion on the membrane surface. Osmosis then acts to dilute regions of solute accumulation and concentrate regions of solute depletion. This occurs by a reduction of the outgoing transmembrane flow in regions of accumulation and an increase of the transmembrane flow in regions of depletion. These variations of the transmembrane flow

in turn likely retroact on the vortices. Assessing this mechanism is the goal of the present work. More specifically, we focus on the question of whether concentration polarization and osmotic pressure act in favor or against the formation of vortices. The subsequent question of whether vortices increase or decrease the average transmembrane flow is left for future work.

This Taylor–Couette configuration provides a unique “test-bed” with which we can control, observe, and study the interactions between vortices, concentration polarization, and osmotic pressure. First, the characteristics of the concentration polarization layer can be controlled by imposing the radial flow, independently of the azimuthal flow driven by the rotation of the inner cylinder. Second, the appearance of vortices due to a centrifugal instability can be easily controlled by setting the rotation rate of the inner cylinder. These centrifugal instabilities and their critical conditions are well studied and understood and we show that our specific configuration also admits a simple analytical solution for the base-state, which permits an analytical stability analysis and a parametric study of the vortices. Finally, the straightforward geometry allows complementary Direct Numerical Simulations using high-order spectral methods.

Our particular configuration is of limited practical use for filtration, because the amount of solvent extracted through one cylinder is balanced by that entering through the other. In industry, rotating filtration processes based on Taylor–Couette cells have a stationary impermeable outer cylinder and a rotating semi-permeable inner cylinder. Feed is pumped axially through the gap while solvent exits the inner cylinder. Though this mode of filtration has niche applications in separating blood plasma from cells, its poor membrane-surface to volume ratio and complicated moving parts make it unrealistic for industrial RO (Hallström & Lopez-Leiva 1978; Margaritis & Wilke 1978; Kroner & Nissinen 1988; Ohashi *et al.* 1988; Beaudoin & Jaffrin 1989; Belfort *et al.* 1993*a,b*; Lueptow & Hajiloo 1995; Schuille *et al.* 2002).

Taylor–Couette flow and its various regimes have been widely studied experimentally, numerically and analytically (see discussions and references in Taylor 1923; Coles 1965; Cole 1976; Davey *et al.* 1968; Marcus 1984; Andereck *et al.* 1986; Koshmieder 1993; Bilson & Bremhorst 2007; Ostilla-Monico *et al.* 2014, among many others). The current work considers cases where the outer cylinder remains stationary. We also focus on the initial transition from steady flow to toroidal vortices, the stability of which is known to be retrieved by linear stability analysis. The stability of a Taylor–Couette cell filled with pure solvent, with a stationary outer cylinder and a superimposed radial flow through both cylinders was first considered by Bahl (1970). For narrow gaps, linear stability analyses (Min & Lueptow 1994; Martinand *et al.* 2017) and direct numerical simulations (Serre *et al.* 2008) show that a radial inflow or strong radial outflow have a stabilizing effect, while a small radial outflow has a slightly destabilizing effect for the first transition from non-vortical to vortical flows. Extending the analysis to large gaps, Martinand *et al.* (2017) found that a strong radial outflow can select pairs of counter-propagating helical vortices, and a strong radial inflow tends to squeeze the vortices against the inner cylinder and dramatically shrink their cross-section in a meridional plane. Weakly non-linear analyses and numerical simulations (Martinand *et al.* 2017) also found that a strong radial outflow or inflow modified the usual supercritical transition to a subcritical transition, exhibiting a hysteresis cycle.

To date, the above analytical and numerical results have all been obtained by imposing a prescribed radial velocity to the base flow, while simultaneously prescribing a no-penetration condition, i.e. a zero radial velocity, to the instabilities. This assumption neglects the potential for flow instabilities to penetrate into the permeable surfaces, which has been shown to destabilize channel and boundary layer flows.

The mixing and transport properties of Taylor vortices have been studied both from a fundamental point of view (Akonur & Lueptow 2002; Nemri *et al.* 2013) and for practical applications (Miyashita & Senna 1993; Giordano *et al.* 2000*a,b*; Aljishi *et al.* 2013). Nevertheless, no studies to date have considered the boundary conditions associated with the rejection of the solute at a membrane and the build-up of a concentration boundary layer together with osmotic pressure. The coupling between transmembrane flow and osmotic pressure has been modeled and studied in boundary layers or channel flows (Haldenwang *et al.* 2010; Lopes *et al.* 2012; Bernales *et al.* 2017). But these works have focused on laminar flows within the Prandtl approximation, thus excluding the possibility of vortical flows.

The article is organized as follows. Section 2 presents the geometry, governing equations, and base-state. Section 3 describes the linear stability analysis and the numerical methods. Section 4 first demonstrates the impact of osmotic pressure on centrifugal instabilities by presenting converging numerical and analytical results (§4.1) then quantitatively assesses over a relevant parameter space the magnitude of this impact on the critical conditions (§4.2) and spatial structures (§4.3) of the instabilities. Section 5 further explains how the semi-permeable membrane and the related velocity and concentration boundary conditions generate this effect. Section 6 sums up our results by expressing analytically the range of parameters over which osmosis impacts the instabilities and the magnitude of this impact as a function of the radius ratio only. Section 7 discusses the interest and limitations of the set-up and presents possible future works.

2. Geometry, governing equations, and base-state

We consider a Taylor–Couette cell with a stationary outer cylinder of radius r_2 , and a concentric inner cylinder of radius r_1 . The inner cylinder rotates about its longitudinal axis with constant angular velocity Ω , as sketched in figure 2. The flow of interest occurs in the annular gap $r_1 \leq r \leq r_2$, which is filled with an incompressible Newtonian solution composed of a solvent (water) and solute. Hereinafter, we use cylindrical coordinates $\mathbf{x} = (r, \theta, z)$, in which the fluid velocity vector is denoted $\mathbf{V} = (U, V, W)^t$, where U , V and W are the radial, azimuthal and axial components, respectively. The fluid pressure is denoted P . The concentration is denoted C , and expressed in mol/m^3 .

The inner and outer cylinders are both semi-permeable membranes of thickness h , through which only the solvent can flow. The inner membrane surrounds a cavity ($r < r_1 - h$) filled with solvent maintained at constant pressure P_{in} . Similarly, the region beyond the outer membrane ($r > r_2 + h$) is filled with solvent maintained at constant pressure P_{out} . The pressure difference between these cavities,

$$\Delta P = P_{\text{in}} - P_{\text{out}}, \quad (2.1)$$

drives radial flow through the annular gap. A positive ΔP drives flow in the positive radial direction, with solvent entering the inner cylinder and leaving the outer cylinder. This causes solute accumulation at the outer cylinder. A negative ΔP drives flow in the negative radial direction, causing solutes to accumulate at the inner cylinder.

Both membrane surfaces satisfy the no-slip condition for the tangential velocity components V and W

$$V|_{r=r_1} = \Omega r_1, \quad W|_{r=r_1} = V|_{r=r_2} = W|_{r=r_2} = 0. \quad (2.2)$$

Radial solvent flow through the inner membrane satisfies a boundary condition involving the transmembrane pressure difference and transmembrane concentration difference in

the form of an osmotic pressure given by van't Hoff's law:

$$U|_{r=r_1} = K \left(P_{\text{in}} - P|_{r=r_1} + RTC|_{r=r_1} \right), \quad (2.3)$$

where K is the membrane permeance to water in the wall-normal direction, defined as the transmembrane velocity of solvent per unit pressure difference, R is the ideal gas constant, and T is the fluid temperature, assumed constant. Similarly, solvent flow through the outer cylinder satisfies

$$U|_{r=r_2} = -K \left(P_{\text{out}} - P|_{r=r_2} + RTC|_{r=r_2} \right). \quad (2.4)$$

Flows over permeable surfaces may have a non-zero tangential velocity at the surface due to momentum transfer to the fluid within the porous material (see Beavers & Joseph 1967). This tangential velocity is important when a streamwise pressure gradient drives a streamwise flow within the porous material. In filtration flow, the no-slip assumption (2.2) is reasonable, because the permeability (or the permeance in our case) is very small, and the membrane very thin. Consequently, the transmembrane pressure gradient, i. e. the transmembrane pressure difference over the membrane thickness, necessary to drive even a small transmembrane velocity is several orders-of-magnitude higher than any pressure gradient tangent to the wall. For systems in which the no-slip assumption is invalid, porous surfaces should be modeled using appropriate momentum transfer condition (see Beavers & Joseph 1967), but to the best of our knowledge, such conditions have never been numerically and/or analytically implemented and assessed in filtration set-ups.

The absence of any solute flux through the inner and outer cylinders requires radial advection and diffusion of solutes to sum to zero at r_1 and r_2 ,

$$\left[UC - \mathcal{D} \frac{\partial C}{\partial r} \right]_{r=r_1} = \left[UC - \mathcal{D} \frac{\partial C}{\partial r} \right]_{r=r_2} = 0, \quad (2.5)$$

where \mathcal{D} is the solute molecular diffusivity. It is worth stressing here that the no-flux boundary condition (2.5) has a non-linear term, UC .

There is no applied axial pressure gradient and, equivalently, no net axial fluid flow. As a consequence, the mass flow rate entering the gap through one of the cylinders balances that leaving through the other, leading to

$$r_1 \langle U \rangle_{r_1} = r_2 \langle U \rangle_{r_2}, \quad (2.6)$$

where $\langle U \rangle_{r_i}$ denote the radial velocities averaged over the inner ($i = 1$) and outer ($i = 2$) cylinders. Due to this balance in radial mass flow rates, solute accumulation at one cylinder is balanced by depletion at the other, such that the solute concentration C_0 averaged over the full domain remains constant. This configuration allows us to control all the physical mechanisms of interest in this study, i.e. the build up of a concentration boundary layer, the coupling between the osmotic pressure and transmembrane flow, and the driving of hydrodynamic instabilities.

2.1. Non-dimensional parameters and equations

Fluid flow and solute transport in the gap are governed by the incompressible continuity, Navier-Stokes and advection-diffusion equations. These are non-dimensionalized using the gap width $d = r_2 - r_1$ for the characteristic length, ν/d for the characteristic velocity, d^2/ν for the characteristic time, $\rho\nu^2/d^2$ for the characteristic pressure, and the average concentration C_0 for the characteristic concentration, where ρ is the fluid density and ν its kinematic viscosity. Hereinafter, all expressions are non-dimensional,

unless otherwise stated. The governing equations may be expressed as

$$\begin{aligned}\nabla \cdot \mathbf{V} &= 0, \\ \frac{\partial \mathbf{V}}{\partial t} + (\mathbf{V} \cdot \nabla) \mathbf{V} &= -\nabla P + \nabla^2 \mathbf{V}, \\ \frac{\partial C}{\partial t} + \mathbf{V} \cdot \nabla C &= \frac{1}{\text{Sc}} \nabla^2 C,\end{aligned}\tag{2.7}$$

where $\text{Sc} = \nu/D$ is the Schmidt number. Boundary conditions are now expressed at the non-dimensional inner and outer radii $r_1 = \eta/(1-\eta)$ and $r_2 = 1/(1-\eta)$, respectively. The boundary conditions for the tangential velocity components can be expressed as

$$V|_{r=r_1} = \text{Ta}, \quad W|_{r=r_1} = V|_{r=r_2} = W|_{r=r_2} = 0,\tag{2.8}$$

where $\text{Ta} = r_1 \Omega d/\nu$ is the Taylor number. The boundary conditions for U and C at the cylinder are written as

$$U|_{r=r_1} = \sigma \left(P_{\text{in}} - P|_{r=r_1} \right) + \chi C|_{r=r_1},\tag{2.9a}$$

$$U|_{r=r_2} = -\sigma \left(P_{\text{out}} - P|_{r=r_2} \right) - \chi C|_{r=r_2},$$

$$\left[\text{Sc} UC - \frac{\partial C}{\partial r} \right]_{r=r_1} = \left[\text{Sc} UC - \frac{\partial C}{\partial r} \right]_{r=r_2} = 0.\tag{2.9b}$$

The semi-permeable nature of the membrane and its permeance K manifest through two independent non-dimensional coefficients in boundary conditions (2.9a): the velocity-pressure coupling coefficient $\sigma = K\rho\nu/d$ and the velocity-concentration coupling coefficient $\chi = KRTdC_0/\nu$. Lastly, the averaged transmembrane velocities are expressed in terms of the Reynolds number

$$\text{Re} = \frac{r_1 \langle U \rangle_{r_1}}{\nu} = \frac{r_2 \langle U \rangle_{r_2}}{\nu}.\tag{2.10}$$

Though this set-up is not commonly used in industrial RO or nanofiltration devices, we nonetheless establish the ranges of the non-dimensional parameters that would prevail in a RO Taylor–Couette cell with semi-permeable cylinders and filled with seawater. In typical seawater plate-and-frame RO systems, the transmembrane velocity is of order 10^{-6} m/s for operating pressure ranging from 5 to 8 MPa, with the osmotic pressure being around 3 MPa. The permeance K of these membranes is of order 10^{-13} to 10^{-12} m/s/Pa (see Table 1 in van Wagner *et al.* 2009, for examples of commercial RO membranes). Assuming arbitrarily the radii r_1 and r_2 are of order 10^{-2} to 10^{-1} m, and the gap width d is of order 10^{-3} to 10^{-2} m, produces velocity-pressure coupling coefficients and Reynolds numbers ranging between $10^{-14} < \sigma < 10^{-12}$ and $10^{-2} < \text{Re} < 10^{-1}$, respectively. Assuming seawater at 25 °C, with an average salt concentration $C_0 \approx 10^3$ mol/m³, produces velocity-concentration coupling coefficients ranging between $10^{-3} < \chi < 10^{-1}$. Considering that D for monovalent ions such as Na⁺ and Cl⁻ is of order 10^{-9} m²/s, the Schmidt number is of order 10^3 . Typical transitional Taylor numbers $\text{Ta} \sim 100$ then correspond to rotation rates Ω ranging from 10^{-1} to 10 rad/s.

2.2. Steady base-state

Equations (2.7)–(2.9) admit a steady, axially and azimuthally invariant base-state $[\mathbf{V}_b(r), P_b(r), C_b(r)]$, the expression of which is given in Appendix A. These velocity and pressure fields are parameterized by Ta and Re solely. Positive values of Re produce

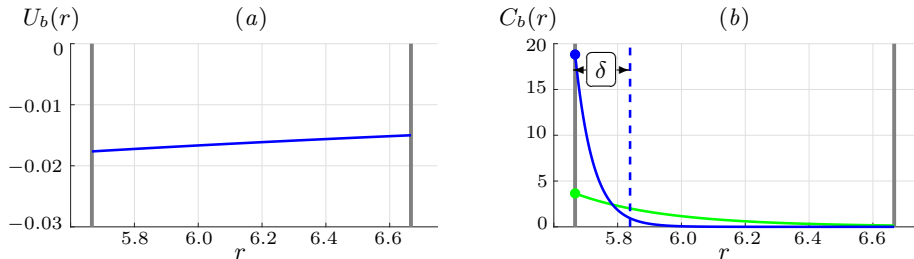


FIGURE 3. (a): Radial velocity of the base-state $U_b(r)$ for radius ratio $\eta = 0.85$ and radial inflow $\text{Re} = -0.1$. (b): Concentration field of the base-state $C_b(r)$ for radius ratio $\eta = 0.85$ a radial inflow with Péclet number $\text{Pe} = \text{ReSc} = -20$ (light grey, green online) and $\text{Pe} = \text{ReSc} = -100$ (dark grey, blue online). The vertical dashed (blue online) line materializes the polarization layer thickness δ as computed from (2.15) for $\text{Pe} = -100$.

a radial velocity $U_b > 0$ flowing outwards, while $\text{Re} < 0$ produces radial velocities $U_b < 0$ flowing inwards, as seen in figure 3(a) for $\text{Re} = -0.1$. By writing the base-state in this form, we apply the Reynolds number Re directly, and then compute the necessary operating pressure (2.1) from boundary conditions (2.9a),

$$\Delta P = P_b(r_1) - P_b(r_2) + \frac{\chi}{\sigma} [C_b(r_2) - C_b(r_1)] + \frac{1}{\sigma} [U_b(r_2) + U_b(r_1)]. \quad (2.11)$$

To further interpret the concentration boundary layer, the base-state C_b in equation (A 4) can be re-expressed in terms of the radius ratio $\eta = r_1/r_2$ and the Péclet number associated with the radial transmembrane flow $\text{Pe} = \text{ReSc}$

$$C_b(r) = \frac{\text{Pe} + 2}{2} \frac{1 - \eta^2}{1 - \eta^{\text{Pe}+2}} (1 - \eta)^{\text{Pe}} r^{\text{Pe}} \quad \text{for } \text{Pe} \neq -2. \quad (2.12)$$

Figure 3(b) shows two examples of C_b when $\eta = 0.85$ with Péclet numbers $\text{Pe} = -20$ (light grey, green online) and $\text{Pe} = -100$ (dark grey, blue online). As Pe increases in absolute value, whether by increasing the Reynolds or the Schmidt numbers, the solute accumulates in an increasingly thin boundary layer near the inner membrane. Simultaneously, pure solvent entering through the outer cylinder depletes the solute concentration outside the polarization layer. To characterize the base-state polarization layer, we first compute the maximum concentration $C_{b,\max}$ (shown as dots in figure 3), which occurs on the membrane surface. We then define the polarization layer thickness δ as the radial distance from the membrane where the concentration is $0.05C_{b,\max}$. Depending on the direction of the radial flow, $C_{b,\max}$ is obtained from (2.12) as

$$C_{b,\max} = \begin{cases} C_b(r_1) = \frac{-(\text{Pe} + 2)}{2} \frac{1 - \eta^2}{1 - \eta^{-(\text{Pe}+2)}} \frac{1}{\eta^2} & \text{for } \text{Pe} < 0 \\ C_b(r_2) = \frac{\text{Pe} + 2}{2} \frac{1 - \eta^2}{1 - \eta^{\text{Pe}+2}} & \text{for } \text{Pe} > 0 \end{cases} \quad (2.13)$$

and, combined to (2.12), leads to

$$\delta = \begin{cases} \left(0.05^{1/\text{Pe}} - 1\right) \frac{\eta}{1 - \eta} & \text{for } \text{Pe} < 0 \\ \left(1 - 0.05^{1/\text{Pe}}\right) \frac{1}{1 - \eta} & \text{for } \text{Pe} > 0. \end{cases} \quad (2.14)$$

For large Péclet numbers (in absolute value), the boundary layer thickness can be

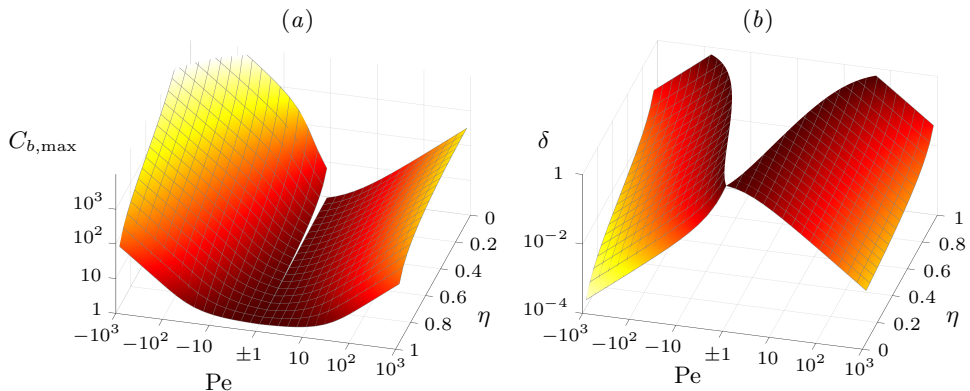


FIGURE 4. (a): Maximum of the concentration field $C_{b,\max}$ (in log scale) as a function of the radius ratio η and Péclet number $Pe = Re Sc$ (in log scale). (b): Boundary layer thickness δ (in log scale) as a function of the radius ratio η and Péclet number $Pe = Re Sc$ (in log scale). Note the uncommon Pe -axis merging negative and positive values of this parameter to account for radial in- and outflows, and the resulting discontinuities of the surfaces. Note also the reversed η -axes in both figures.

approximated by

$$\delta \approx \begin{cases} \frac{\log(20)}{-Pe} \frac{\eta}{1-\eta} & \text{for } Pe < 0 \\ \frac{\log(20)}{Pe} \frac{1}{1-\eta} & \text{for } Pe > 0, \end{cases} \quad (2.15)$$

and is inversely proportional to the Péclet number. Figure 4 shows $C_{b,\max}$ and δ as functions of the radius ratio η and Péclet number Pe , where $Pe < 0$ represents radial inflow and $Pe > 0$ represents radial outflow. Maximum non-dimensional concentrations beyond 10^3 are not depicted, because these would likely trigger solute precipitation and call the governing equations into question. Non-dimensional boundary layer thicknesses above 1 are not shown because this would correspond to layers larger than the gap. For $\delta > 1$, one can assume that no boundary layer forms. As expected, increasing the magnitude of the Péclet number reduces the boundary layer thickness δ and increases the maximum concentration $C_{b,\max}$. Decreasing the radius ratio η , by reducing the radii r_1 and r_2 , increases the magnitude of the velocities $U_b(r_1)$ and $U_b(r_2)$ for a prescribed Péclet number. It thus reduces the boundary layer thickness δ and increases the maximum concentration $C_{b,\max}$. Note that for a given Péclet number, the magnitude of the radial velocity through the inner cylinder always exceeds that through the outer, because $U_b(r_1) = U_b(r_2)/\eta$. Consequently, in figure 4(a), the solute concentration on the inner cylinder is greater than that on the outer cylinder. Accordingly, in figure 4(b), the boundary layer at the inner cylinder is thinner than that on the outer cylinder.

The base-state (A1–A4) does not present any dependence on the velocity-concentration coupling coefficient χ and velocity pressure coupling-coefficient σ , as these parameters only affect the operating pressure (2.11). This operating pressure is of major practical importance because it imposes the non-dimensional power per unit axial length needed to drive the fluid across the Taylor–Couette cell: $\mathcal{P} = 2\pi Re \Delta P$. The impact of system design and operating conditions on ΔP can be understood by investigating each term in expression (2.11), repeated below for convenience

$$\Delta P = P_b(r_1) - P_b(r_2) + \frac{\chi}{\sigma} [C_b(r_2) - C_b(r_1)] + \frac{1}{\sigma} [U_b(r_2) + U_b(r_1)]. \quad (2.16)$$

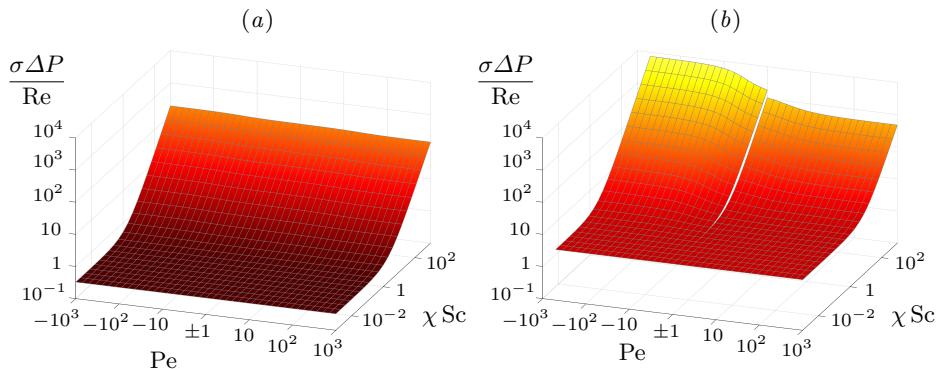


FIGURE 5. Reduced operating pressure $\sigma\Delta P/\text{Re}$ as a function of χSc and $\text{Pe} = \text{ReSc}$, for (a): $\eta = 0.85$ and (b): $\eta = 0.25$. All quantities are in log scale and note the uncommon Pe -axis merging positive and negative values of this parameter to account for out- and inflows and the resulting discontinuities of the surfaces.

The first term $P_b(r_1) - P_b(r_2)$ is due to hydrodynamics and combines a contribution due to the curvature of the azimuthal flow, scaling with Ta^2 , and a contribution due to the radial flow, scaling with Re^2 , both up to multiplicative functions of η . The next term

$$\frac{\chi}{\sigma} [C_b(r_2) - C_b(r_1)] = \frac{\chi(\text{Pe} + 2)}{2\sigma} \frac{1 - \eta^2}{1 - \eta^{\text{Pe}+2}} (1 - \eta^{\text{Pe}}), \quad (2.17)$$

is due to the osmotic pressure. For large Péclet numbers (in absolute value), it mostly scales with $\chi\text{Pe}\sigma^{-1} = \chi\text{ReSc}\sigma^{-1}$, up to a multiplicative function of η . The last term

$$\frac{1}{\sigma} [U_b(r_2) + U_b(r_1)] = \frac{\text{Re}}{\sigma} \frac{1 - \eta^2}{\eta}, \quad (2.18)$$

is due to the transmembrane flow of solvent and scales with $\text{Re}\sigma^{-1}$, up to a multiplicative function of η . Typical membrane filtration conditions present very small σ , such that the hydrodynamic term in the operating pressure (2.11) is negligible compared to the two next terms, i. e. the operating pressure is mostly imposed by the membrane permeance and osmotic pressure. Neglecting the hydrodynamic terms leads to the approximation

$$\frac{\sigma\Delta P}{\text{Re}} \approx \frac{1 - \eta^2}{\eta} \left(1 + \frac{\chi\text{Sc}(\text{Pe} + 2)}{2\text{Pe}} \eta \frac{1 - \eta^{\text{Pe}}}{1 - \eta^{\text{Pe}+2}} \right), \quad (2.19)$$

depicted in figure 5 for narrow ($\eta = 0.85$) and wide ($\eta = 0.25$) gaps. For narrow gaps, this operating pressure is almost independent of the Péclet number. For wide gaps, the operating pressure becomes substantially stronger for inflows than for outflows, due to the strong discrepancy between the transmembrane velocities at the inner and outer cylinders.

3. Analytical and numerical methods

We explore the appearance of vortical flow structures and their coupling with concentration polarization by performing a linear stability analysis of the base-state. We also perform complementary direct numerical simulations of the complete flow fields.

3.1. Linear stability analysis

The stability analysis decomposes the flow fields into the sum of the base-state $[\mathbf{V}_b, P_b, C_b]$ and small perturbations $[\mathbf{V}_p(\mathbf{x}, t), P_p(\mathbf{x}, t), C_p(\mathbf{x}, t)]$. Linearizing equations (2.7) about the base-state produces the following evolution equations for the small perturbation,

$$\begin{aligned} \nabla \cdot \mathbf{V}_p &= 0, \\ \frac{\partial \mathbf{V}_p}{\partial t} + \mathbf{V}_b \cdot \nabla \mathbf{V}_p + \mathbf{V}_p \cdot \nabla \mathbf{V}_b &= -\nabla P_p + \nabla^2 \mathbf{V}_p, \\ \frac{\partial C_p}{\partial t} + \mathbf{V}_b \cdot \nabla C_p + \mathbf{V}_p \cdot \nabla C_b &= \frac{1}{\text{Sc}} \nabla^2 C_p. \end{aligned} \quad (3.1)$$

The linearization of boundary conditions (2.9) produces

$$V_p \Big|_{r=r_i} = W_p \Big|_{r=r_i} = 0, \quad (3.2a)$$

$$U_p \Big|_{r=r_i} = \mp [\sigma P_p - \chi C_p] \Big|_{r=r_i}, \quad (3.2b)$$

$$\left[U_p C_b + U_b C_p - \frac{1}{\text{Sc}} \frac{\partial C_p}{\partial r} \right] \Big|_{r=r_i} = 0, \quad (3.2c)$$

where $r_i = r_1$ or r_2 , and the negative (positive) sign in condition (3.2b) is used when $r = r_1$ ($r = r_2$). Note that the terms $U_p C_b$ and $U_b C_p$ in the no-flux condition (3.2c) arise from the linearization of the solute advection term UC in condition (2.5).

Our stability analysis considers perturbations of the form

$$[\mathbf{V}_p(\mathbf{x}, t), P_p(\mathbf{x}, t), C_p(\mathbf{x}, t)] = [\mathbf{v}_p(r), p_p(r), c_p(r)] \exp(ikz + in\theta + st), \quad (3.3)$$

where k and n are the axial and azimuthal wavenumbers, respectively, s is the growth rate, and $[\mathbf{v}_p(r), p_p(r), c_p(r)]$ are radial profiles, describing the variation of the perturbation structures in the radial direction. Substituting form (3.3) into the linearized equations (3.1)–(3.2) produces a generalized eigenvalue problem

$$\mathcal{A}[\mathbf{v}_p, p_p, c_p] = -s\mathcal{B}[\mathbf{v}_p, p_p, c_p], \quad (3.4)$$

for which s and $[\mathbf{v}_p, p_p, c_p]$ are the eigenvalues and eigenvectors, respectively. The differential operators \mathcal{A} and \mathcal{B} are given in Appendix B. The radial profiles satisfy the boundary conditions

$$v_p(r_i) = w_p(r_i) = 0, \quad (3.5a)$$

$$u_p(r_i) = \mp [\sigma p_p(r_i) - \chi c_p(r_i)], \quad (3.5b)$$

$$u_p(r_i) C_b(r_i) + U_b(r_i) c_p(r_i) - \frac{1}{\text{Sc}} \frac{dc_p}{dr}(r_i) = 0, \quad (3.5c)$$

where, again, $r_i = r_1$ or r_2 , and the negative sign in condition (3.5b) is used when $r = r_1$.

The eigenvalue problem is solved using a standard spectral collocation method with a typical resolution of 72 Chebyshev polynomials in the radial direction. Newton–Raphson methods previously explained in Martinand *et al.* (2009) are used to determine the critical conditions of the most unstable mode. This yields the critical Taylor number Ta^{crit} above which the real part of a first eigenvalue s , associated with the eigenmode $[\mathbf{v}_p^{\text{crit}}, p_p^{\text{crit}}, c_p^{\text{crit}}]$ with axial wavenumber k^{crit} and azimuthal wavenumber n^{crit} , becomes positive.

3.2. Direct numerical simulations

We perform axisymmetric Direct Numerical Simulations (DNS) of equations (2.7)–(2.9) using an in-house pseudo-spectral code previously detailed in Tilton *et al.* (2014). The code has been successfully used to simulate tubular membrane filtration systems (Tilton *et al.* 2012), and steady (Tilton *et al.* 2010) and unsteady (Tilton & Martinand 2018) flows in Taylor–Couette–Poiseuille cells with permeable inner cylinders and pure solvent, and has been modified to include the resolution of the scalar equation and boundary conditions (2.9). The code discretizes the radial and axial directions using Chebyshev polynomials, and uses a second-order semi-implicit temporal scheme suggested by Vanel *et al.* (1986). The pressure solver is based on the projection method introduced in Raspo *et al.* (2002) and extended in Tilton *et al.* (2014) to satisfy the velocity-pressure and velocity-concentration couplings on the semi-permeable membranes. We simulate a domain of non-dimensional axial length $L = 20$ with 36 and 148 collocation points in the radial and axial directions, respectively. Spatial convergence is confirmed by monitoring the Chebyshev expansion coefficients. The base flow $\mathbf{V}_b(r)$ in Appendix A is imposed at both axial ends of the domain, so that no net axial flow exists and the conservation of the total radial flux (2.10) is satisfied. Moreover, the concentration field satisfies vanishing Neumann boundary conditions at those two axial ends, so that the average concentration in the domain is conserved. The initial conditions are composed of a small disturbance added to the analytical base-state (A 1–A 4). To reduce the simulation time, the initial disturbance takes the form of the analytically computed marginal mode $[\mathbf{V}_p^{\text{crit}}, P_p^{\text{crit}}, C_p^{\text{crit}}]$ with an arbitrarily small amplitude. This was implemented after first verifying that disturbances in this form or in the form of white noise on the axial velocity led to the same final flow. For the supercritical Taylor numbers considered, we found that perturbation growth eventually saturated such that all simulations settled to steady-states.

4. Taylor vortices and osmotic pressure

Using linear stability analysis and DNS, the dynamics of Taylor vortices is now addressed. More specifically, we focus on the impact of osmosis on the critical conditions above which the vortices develop, and on the velocity and concentration fields of the perturbation.

4.1. Numerical and analytical results at $\eta = 0.85$, $\text{Pe} = 100$ and $\chi = 10^{-3}$

Figure 6 shows the steady radial velocity $U(r, z)$ and concentration field $C(r, z)$ obtained by DNS for a radial inflow of $\text{Re} = -0.1$, velocity-pressure coupling coefficient $\sigma = 10^{-10}$, Schmidt number $\text{Sc} = 1000$, and velocity-concentration coupling coefficient $\chi = 10^{-3}$, in a narrow-gap cell with $\eta = 0.85$ at $\text{Ta} = 90$. A full analysis of the numerical flow fields $[\mathbf{V}^{\text{num}}, P^{\text{num}}, C^{\text{num}}]$ shows that these fields are composed of the base-state and a perturbation in the form of toroidal counter-rotating vortices with an axial wavelength $\lambda \approx 2.5$. These vortices present a non-zero radial velocity at the inner cylinder. The order of magnitude of this transmembrane velocity is comparable to the order of magnitude of the radial velocity of the vortices observed in the bulk of the flow. Together with these vortices, the concentration field exhibits substantial fluctuations with the same aforementioned axial wavelength. These fluctuations are mostly observed within the polarization layer, whose width $\delta = 0.171$ is computed from (2.15), and located between the inner cylinder and the superimposed dashed curve in figure 6(b). A similar DNS at Taylor number $\text{Ta} = 78$ (not shown here) retrieved the base-state, free

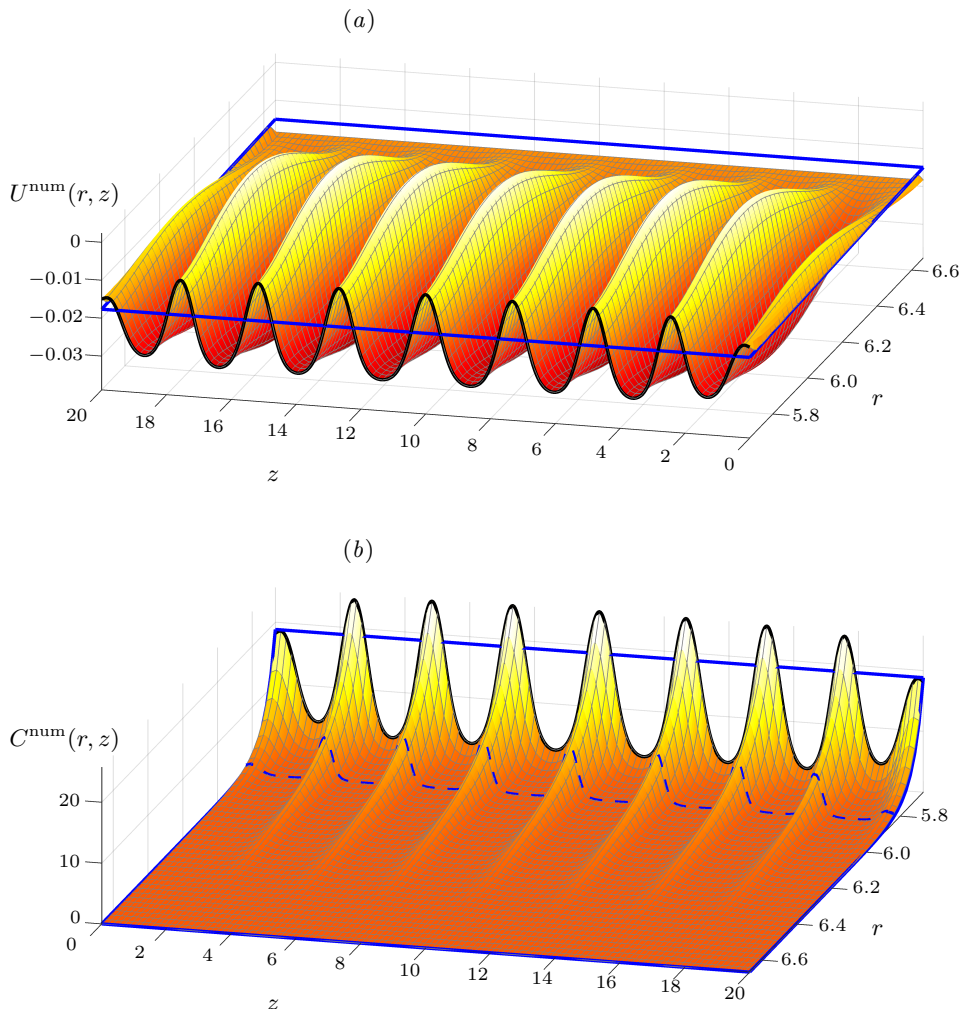


FIGURE 6. (a): Radial velocity field U^{num} and (b): concentration field C^{num} as functions of r and z , obtained by Direct Numerical Simulations for $\eta = 0.85$, $\text{Re} = -0.1$, $\sigma = 10^{-10}$, $\text{Sc} = 1000$ and $\chi = 10^{-3}$, at $\text{Ta} = 90$. The black superimposed curves highlight the fluctuations of radial velocity and concentration at the membrane. The dark grey (blue online) frames on both surfaces are a reminder of the base-state U_b and C_b and the dark grey (blue online) dashed curve superimposed to the concentration field bounds the polarization layer, the thickness of which δ is given by (2.15). Note that for the sake of clarity, the r -axis has been reversed between both surfaces.

of any vortex. For this set of parameters ($\eta = 0.85$, $\text{Re} = -0.1$, $\sigma = 10^{-10}$, $\chi = 10^{-3}$), the linear stability analysis predicts $\text{Ta}^{\text{crit}} = 79.1$ and $\lambda^{\text{crit}} = 2.26$, in good agreement with the DNS. The non-zero critical Taylor number means that the centrifugal force remains the necessary ingredient to the development of the vortices. If we remove osmotic pressure effects by setting $\chi = 0$ (by assuming, for instance, that the reference physical concentration C_0 tends to 0), the stability analysis predicts for Taylor vortices slightly modified by the radial inflow $\text{Ta}^{\text{crit}} = 106.9$ and $\lambda^{\text{crit}} = 2.04$: the presence of osmotic pressure dramatically decreases the critical Taylor number, together with increasing the wavelength of the vortices.

To compare the numerical and analytical results for the perturbation velocity and concentration, the DNS hereinafter is performed closer to critical conditions at $Ta = 80$, and considered at a time before the steady state, shown in Figure 6, is reached, so that the growth of the instability is still in its linear dynamic. Figure 7 first shows the velocity and concentration fields of the perturbation in a meridional plane, in the form of the numerical velocity and concentration fields, $(U_p^{\text{num}}(r, z), W_p^{\text{num}}(r, z))$ and $C_p^{\text{num}}(r, z)$, obtained by removing the base-state $[\mathbf{V}_b, P_b, C_b]$ from the complete DNS fields $[\mathbf{V}^{\text{num}}, P^{\text{num}}, C^{\text{num}}]$ (panel *a*), together with the analytical fields, $(U_p^{\text{crit}}(r, z), W_p^{\text{crit}}(r, z))$ and $C_p^{\text{crit}}(r, z)$ (panel *b*). The focus being on the linear dynamic of the instabilities, the amplitudes of the perturbations are reset so that the maxima of the analytical and numerical azimuthal velocity components are both normalized to 1.

The numerical and analytical fields compare favorably and further ascertain the validity of both approaches. Figure 7 also sheds light on the coupling between the vortices, concentration boundary layer, and osmotic pressure. The non-zero boundary condition at the inner cylinder for the radial velocity of the perturbation is obvious, and extra extraction of fluid at the inner cylinder (related to the perturbation, in addition to the radial mean flow) is found to coincide with the inward jets of the vortices in the bulk. Symmetrically, extra injection of fluid at the inner cylinder is found to coincide with the outward jets of the vortices in the bulk. Moreover, it can be seen that injections/outward jets occur at the axial locations where the perturbation develops an excess of solute, whereas extractions/inward jets occur at the axial locations where the perturbation depletes the solute. From these observations, a mechanism by which osmotic pressure retroacts on the vortices can be proposed. The regions of excess of solute act via osmotic pressure to add extra injection of pure solvent in the bulk through the inner cylinder, thus reinforcing the outward jets of the vortices. Similarly, regions of depleted solute add extra extraction of pure solvent from the bulk, thus reinforcing the inward jets of the vortices. As far as the perturbation $[\mathbf{V}_p, P_p, C_p]$ is concerned, vortices and osmosis are found to work in a cooperative fashion, and osmotic pressure hence reduces the critical conditions for centrifugal instabilities. Moreover, owing to the non-zero boundary condition for the radial velocity, the vortices “penetrate” into the inner cylinder, and the increased perceived radial characteristic size of a vortex induces an increased axial one to conserve a “round” cross-section, explaining the observed increase of the axial wavelength.

A finer comparison between our numerical and analytical results is obtained by assessing the radial profiles of the perturbation structures. The solid curves (green online) in figures 7(c), (d), (e) and (f) show the analytical results for the critical eigenmode $[\mathbf{v}_p^{\text{crit}}, c_p^{\text{crit}}]$. The dashed curves (blue online) show the corresponding DNS results for $[\mathbf{V}^{\text{num}} - \mathbf{V}_b, C^{\text{num}} - C_b]$, at $Ta = 80$ and the axial location z_{outward} of an outward jet (and between two neighbouring outward and inward jets for for the axial component $w_p(r)$). Beyond the nearly identical radial profiles, the membrane boundary conditions (3.2b) and (3.2c) are accurately captured by both the DNS and linear analysis, but a minute discrepancy, that could not be explained so far, is observed between the two approaches.

4.2. Parametric study by linear stability analysis

The case shown in §4.1 demonstrates that transmembrane flow, concentration polarization and osmotic pressure can substantially decrease the critical Taylor number for the appearance of vortices. The next question is to evaluate whether these phenomena always favor the development of the centrifugal instabilities, and to what extent they impact the critical Taylor number. For that purpose, we use the analytic approach

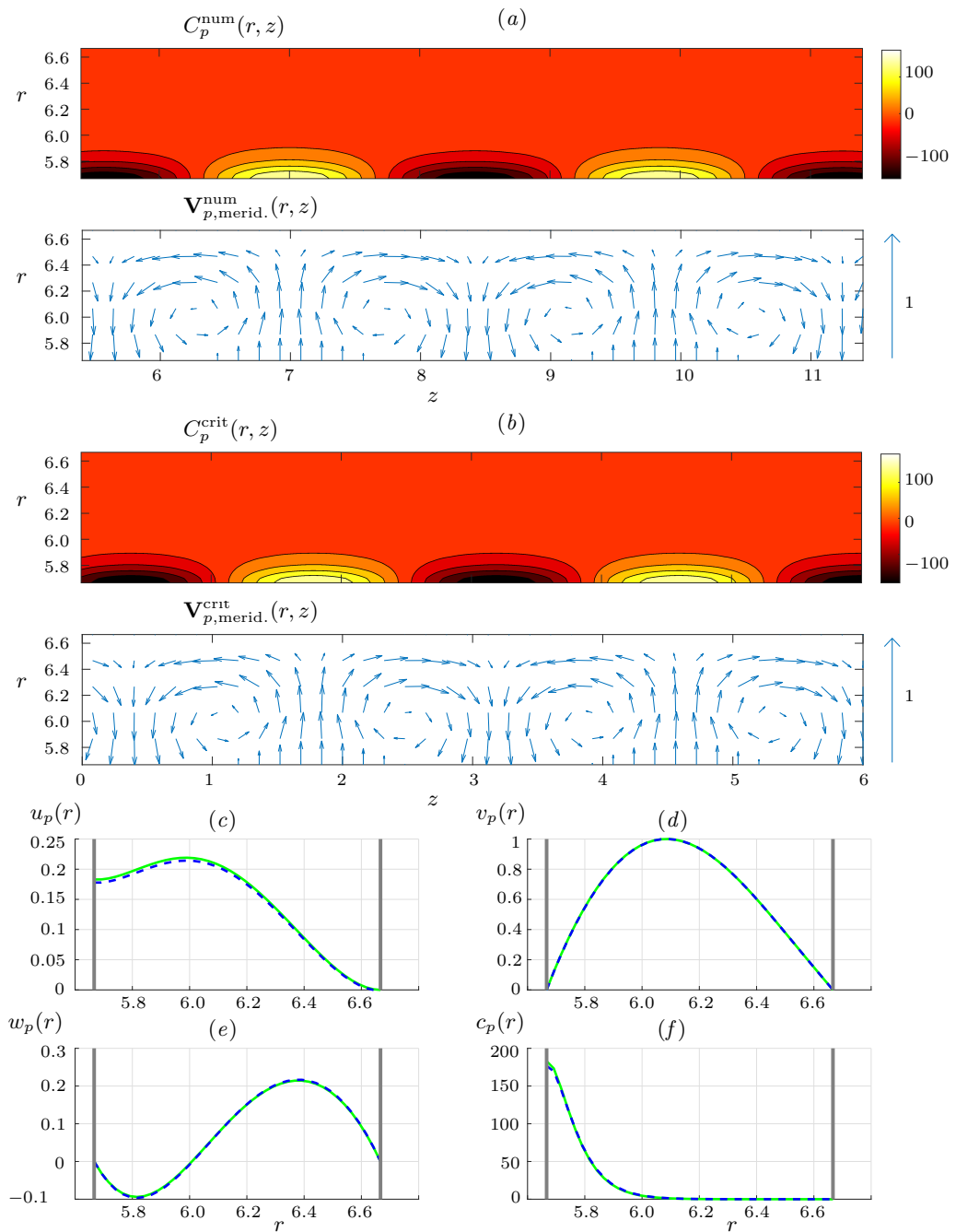


FIGURE 7. Velocity fields of the vortices $\mathbf{V}_{p,\text{merid.}} = (U_p, W_p)$ and concentration perturbation C_p in a meridional plane (r, z) , for $\eta = 0.85$, $\text{Re} = -0.1$, $\text{Sc} = 1000$, $\sigma = 10^{-10}$ and $\chi = 10^{-3}$, obtained numerically at $Ta = 80$ (a) and analytically at critical conditions $Ta^{\text{crit}} = 78.4$ (b). Corresponding radial profiles of the radial (c), azimuthal (d) and axial (e) components of the velocity and concentration (f) perturbations, obtained by linear stability analysis (light grey, green online, solid curves) and DNS (dark grey, blue online, dashed curves).

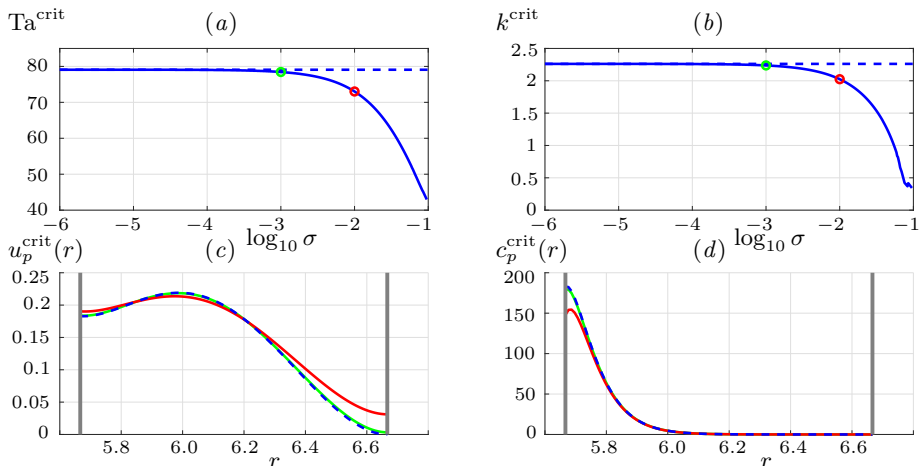


FIGURE 8. Analytically obtained critical Taylor number Ta^{crit} (a) and axial wavenumber k^{crit} (b), in the presence of radial inflow with $Re = -0.1$, for $\eta = 0.85$, $Sc = 10^3$ and $\chi = 10^{-3}$, as functions of the velocity-pressure coupling coefficient σ , in log scale. The dashed horizontal lines correspond to the case where $\sigma = 0$ in boundary conditions (3.2b). Analytically obtained radial profiles of the radial component of the velocity (c) and concentration (d) for $Re = -0.1$, $\eta = 0.85$, $Sc = 10^3$, $\chi = 10^{-3}$, and $\sigma = 0$ (dashed, blue online, curve), $\sigma = 10^{-3}$ (light grey, green online, solid curve) and $\sigma = 10^{-2}$ (dark grey, red online, solid curve).

presented in §3.1 to perform a parametric study considering wide to narrow gap cases with radius ratios varying in the range $0.25 \leq \eta \leq 0.95$, radial Reynolds numbers varying in the range $-1 \leq Re \leq 1$, Schmidt numbers varying in the range $0 \leq Sc \leq 20000$, and velocity-concentration coupling coefficients (scaling the magnitude of the osmotic pressure) varying in the range $10^{-6} \leq \chi \leq 1$. In addition to tracking the critical Taylor number, we explore the effects of osmotic pressure on the geometrical features of the vortices, in terms of wavenumber and radial profiles.

It might be surprising that the velocity-pressure coupling coefficient σ is disregarded in the parametric study. Recall, however, that the base-state $[\mathbf{V}_b, P_b, C_b]$ computed in §2.2 does not depend on σ , because this latter only affects the operating pressure ΔP . In the linear stability problem, σ thus only appears in boundary conditions (3.2b). Figure 8 shows that for $Re = -0.1, Sc = 10^3, \chi = 10^{-1}$ and $\eta = 0.85$, the critical Taylor number Ta^{crit} and axial wavenumber k^{crit} together with the radial profiles of the critical perturbation $u_p^{\text{crit}}(r)$ and $c_p^{\text{crit}}(r)$ are barely affected by a non-zero velocity-pressure coupling coefficient, up to $\sigma \sim 10^{-3}$. More specifically in figures 8(a) and (b), removing the pressure term in boundary conditions (3.5b), i. e. setting $\sigma = 0$, leads to $Ta^{\text{crit}} = 79.1$ and $k^{\text{crit}} = 2.26$ (the asymptotic dashed lines), whereas $\sigma = 10^{-3}$ (the light grey, green online, circles) leads to $Ta^{\text{crit}} = 78.4$ and $k^{\text{crit}} = 2.24$. In figures 8(c) and (d), the radial profiles of the radial velocity component and concentration of the perturbation (the dark grey, blue online, dashed curves for $\sigma = 0$ and the light grey, green online, solid curves for $\sigma = 10^{-3}$) are barely distinguishable. Beyond 10^{-3} , σ noticeably impacts the critical conditions and perturbation. With $\sigma = 10^{-2}$ (the dark grey, red online, circles in figures 8(a) and (b)), $Ta^{\text{crit}} = 73.0$, $k^{\text{crit}} = 2.02$ and the velocity-pressure coupling at the membranes also clearly affects the radial profiles (the dark grey, red online, solid curves in figures 8(c) and (d)). For very weak values of σ typical of RO, the pressure term in boundary conditions (3.2b) can be ignored. As its boundary condition (3.5b) reduces then

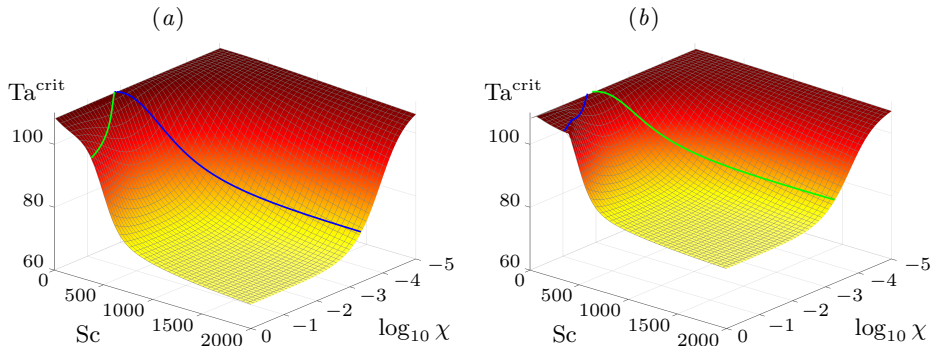


FIGURE 9. Critical Taylor number as a function of the Schmidt number Sc and coupling coefficient χ , in log scale, for $\eta = 0.85$ and $Re = -0.1$ (a) and $Re = 0.1$ (b). The dark grey (blue online) solid curves correspond to the locus of the boundary condition criterion on the inner cylinder χ_1 (5.7) and the light grey (green online) ones to the boundary condition criterion on the outer cylinder χ_2 (5.11).

to

$$u_p(r_i) = \pm \chi c_p(r_i), \quad (4.1)$$

the stability analysis is now completely independent of σ . We stress, however, that the membrane permeance K also enters the velocity-concentration coupling coefficient χ . Our approximation consequently amounts to neglecting the hydrodynamic pressure compared to the osmotic pressure in the transmembrane flow of the perturbation. Our DNS, though, implements the complete boundary conditions (2.9a).

For the full range of parameters considered, the linear critical modes of instability were always in the form of counter-rotating toroidal vortices, i. e. $n^{\text{crit}} \equiv 0$, as depicted in figure 6. To reduce the CPU time, we consequently limit our DNS to axisymmetric computations.

To explore the effect of the osmotic pressure induced by concentration polarization, we begin by considering the impact of the Schmidt number Sc and the coupling coefficient χ , at fixed values of the radius ratio η and radial Reynolds number Re . The salient features are summarized in figure 9, showing Ta^{crit} as a function of the Sc and χ for $\eta = 0.85$ and $Re = -0.1$ (panel a) and $Re = 0.1$ (panel b). As Sc and/or χ are increased, the critical Taylor number Ta^{crit} first substantially decreases, before eventually leveling off. Starting from its value obtained in the case of pure solvent $Ta_{\text{pure}}^{\text{crit}}$, the critical Taylor number tends towards a limit value in conditions where osmosis performs its maximum effect to favor the instabilities. This smooth decrease of Ta^{crit} , and the fact that it never vanishes, support the fact that these instabilities remain driven by the centrifugal force and take the form of altered Taylor vortices, favored by osmotic pressure.

This reinforcement is observed when polarization occurs at the inner cylinder ($Re = -0.1$ in panel a), or at the outer cylinder ($Re = 0.1$ in panel b), but it is more pronounced in the former. Though the critical Taylor number asymptotically tends towards a limit value, we will assume that this limit is almost reached at the minimum of the critical Taylor number $Ta_{\text{min}}^{\text{crit}}$ in the parameter range of this study, i. e. for $Sc < 2000$ and $\chi < 1$. The overall decrease of Ta^{crit} can be quantified by introducing the ratio ϵ :

$$\epsilon = 1 - \frac{Ta_{\text{min}}^{\text{crit}}}{Ta_{\text{pure}}^{\text{crit}}}. \quad (4.2)$$

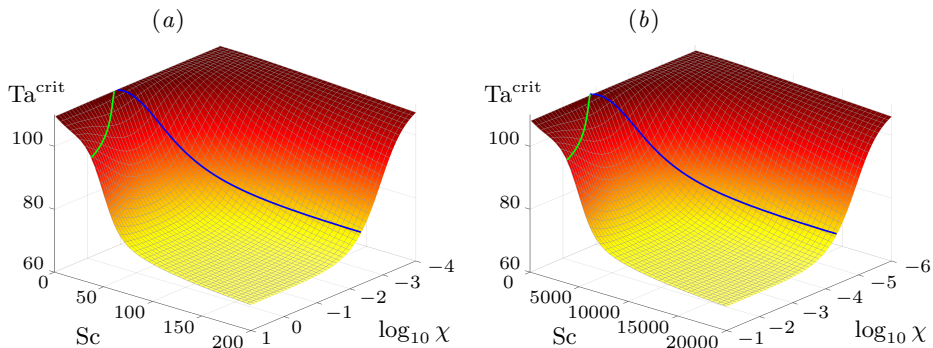


FIGURE 10. Critical Taylor number as a function of the Schmidt number Sc and coupling coefficient χ , in log scale, for $\eta = 0.85$ and $Re = -1$ (a) and $Re = -0.01$ (b). The dark grey (blue online) solid curves correspond to the locus of the boundary condition criterion on the inner cylinder χ_1 (5.7) and the light grey (green online) ones to the boundary condition criterion on the outer cylinder χ_2 (5.11).

Quantitatively, for $\eta = 0.85$ and radial inflow $Re = -0.1$, the critical Taylor number decreases up to $Ta_{\min}^{\text{crit}} = Ta_{\text{Sc}=2000, \chi=1}^{\text{crit}} = 67.6$, compared to $Ta_{\text{pure}}^{\text{crit}} = 108.4$, corresponding to $\epsilon \approx 0.37$. For $\eta = 0.85$ and radial outflow $Re = 0.1$, the critical Taylor number decreases up to $Ta_{\min}^{\text{crit}} = Ta_{\text{Sc}=2000, \chi=1}^{\text{crit}} = 79.0$, compared to $Ta_{\text{pure}}^{\text{crit}} = 108.2$, corresponding to $\epsilon = 0.27$. Section 5 elaborates further on the mechanism by which osmotic pressure, molecular diffusion and Taylor vortices couple and explain in a more detailed fashion the variations of Ta^{crit} with χ .

Figure 10 demonstrates the impact of the magnitude of the imposed radial flow, quantified by the radial Reynolds number Re . Panel (a) shows the critical Taylor number obtained for $\eta = 0.85$ and a strong radial inflow $Re = -1$. The Schmidt number ranges from 0 to 200 and the coupling coefficient χ ranges from 10^{-4} to 10. Panel (b) shows the corresponding results for a weak radial inflow $Re = -0.01$, with Schmidt number ranging from 0 to 20000 and coupling coefficient χ ranging from 10^{-6} to 10^{-1} (panel b). The surfaces shown in figures 9(a), 10(a) and 10(b) clearly collapse under the rescaling $(Re, Sc, \chi) \rightarrow (a^{-1} Re, a Sc, a^{-1} \chi)$, with a an arbitrary constant. The critical conditions thus depend on combinations $(Re Sc, \chi Sc)$ rather than parameters (Re, Sc, χ) .

Figures 11 demonstrates the influence of the radius ratio η on the critical conditions of the vortices. Panel 11(a) shows Ta^{crit} as a function of the Schmidt number Sc and coupling coefficient χ , for a radial inflow $Re = -0.1$, in a narrow gap $\eta = 0.95$. Panel (b) shows the corresponding results in a medium gap $\eta = 0.55$. Variations of η are known to induce large changes in the critical Taylor number in the case of pure solvent. We see these changes are also observed as solute and osmosis are present. In the medium gap ($\eta = 0.55$ in panel b), Taylor vortices appear above $Ta^{\text{crit}} = 40.1$ for $Sc = 2000$ and $\chi = 1$, compared to $Ta_{\text{pure}}^{\text{crit}} = 69.6$ for pure solvent, corresponding to $\epsilon = 0.42$. In the narrow gap ($\eta = 0.95$ in panel a), the critical Taylor number exhibits a novel feature. At fixed Schmidt number, as the coupling coefficient χ is increased, Ta^{crit} first decreases under the effect of osmotic pressure, but eventually increases to recover the value obtained for pure solvent. In this narrow gap, the minimum critical Taylor number is reached for $\chi = 0.023$ instead of $\chi = 1$ for the other cases. The critical Taylor number decreased up to $Ta_{\min}^{\text{crit}} = 131.0$, compared to $Ta_{\text{pure}}^{\text{crit}} = 185.1$, corresponding to $\epsilon = 0.29$.

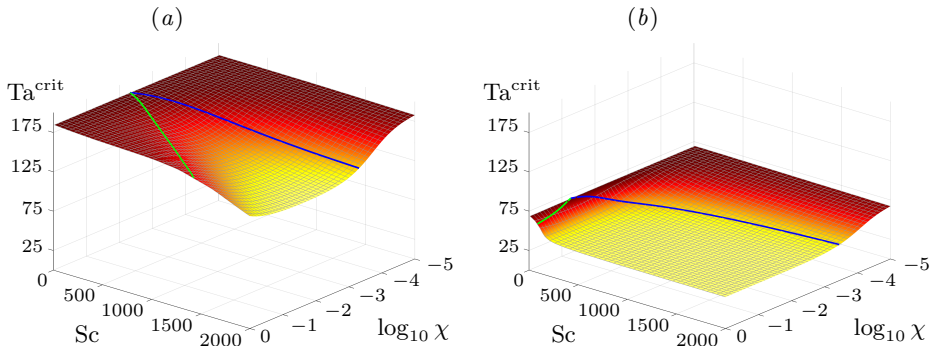


FIGURE 11. Critical Taylor number as a function of the Schmidt number Sc and coupling coefficient χ , in log scale, for $Re = -0.1$ and $\eta = 0.95$ (a) and $\eta = 0.55$ (b). The dark grey (blue online) solid curves correspond to the locus of the boundary condition criterion on the inner cylinder χ_1 (5.7) and the light grey (green online) ones to the boundary condition criterion on the outer cylinder χ_2 (5.11).

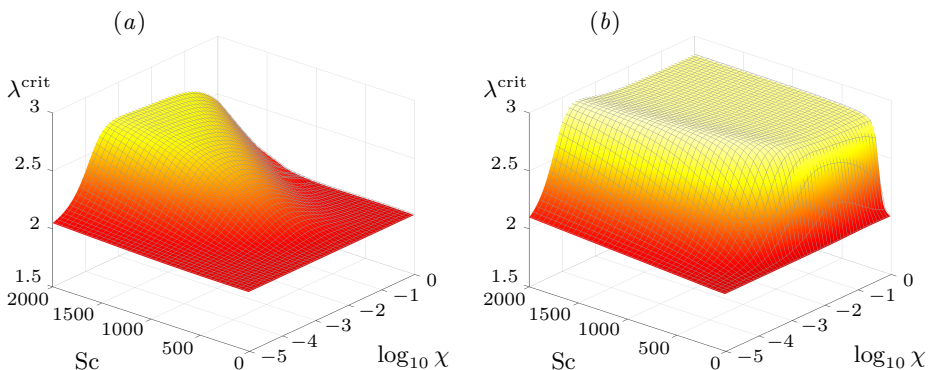


FIGURE 12. Wavelength at critical conditions λ^{crit} , as a function of the Schmidt number Sc and coupling coefficient χ in log scale, for $Re = -0.1$ and $\eta = 0.95$ (a) and $\eta = 0.55$ (b). Note the axes orientation differing from figure 11.

4.3. Velocity and concentration fields of the centrifugal instabilities

Above Ta^{crit} , the centrifugal instabilities take the form of counter-rotating toroidal vortices, with $n^{\text{crit}} = 0$. To investigate how osmotic pressure modifies the structure of these centrifugal instabilities, figure 12 shows the critical axial wavelength $\lambda^{\text{crit}} = 2\pi/k^{\text{crit}}$, as a function of Sc and χ for $\eta = 0.95$ (panel a) and $\eta = 0.55$ (panel b). By comparing figures 11 and 12, conditions for which the critical Taylor number is affected by osmosis are readily found to also increase the characteristic size of the vortices along the axial direction. Similarly, when the effect of osmosis plateaus and the critical Taylor number tends to its limit $Ta_{\text{osm}}^{\text{crit}}$, so does the axial wavelength. At its maximum, the axial wavelength λ^{crit} is increased by almost 50%, in relation with a decreasing critical axial wavenumber k^{crit} .

We further explore the structure of the vortices by considering the perturbation fields $\mathbf{V}_p^{\text{crit}}$ and C_p^{crit} , obtained analytically at Ta^{crit} . In addition to figure 7(b) showing those fields in a meridional plane for $\eta = 0.85$, $\alpha = -0.1$, $\chi = 10^{-2}$, and $Sc = 1000$, figure

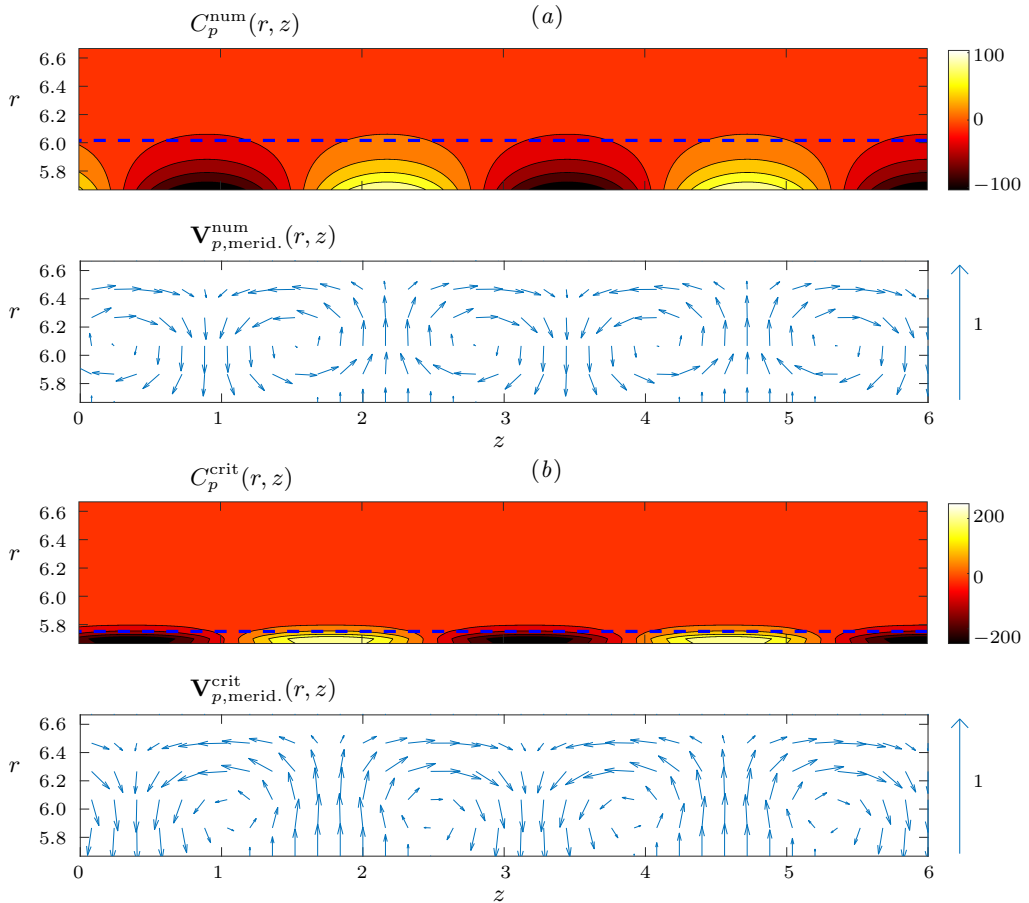


FIGURE 13. Velocity fields of the vortices $\mathbf{V}_{p,\text{merid.}} = (U_p, W_p)$ and concentration perturbation C_p in a meridional plane (r, z) , for $\eta = 0.85$, $\text{Re} = -0.1$, $\chi = 10^{-3}$ and $\text{Sc} = 500$ (a) and $\text{Sc} = 2000$ (b), obtained analytically at critical conditions. The dark grey (blue online) dashed lines above the inner cylinder bound the polarization layer, the thickness of which is given by (2.15).

13 shows them for $\text{Sc} = 500$ (panel a) and $\text{Sc} = 2000$ (panel b). Whereas the vortices are only marginally impacted as molecular diffusion is decreased, the patches of solute accumulation and depletion are found to get thinner along the radial direction, following the similar evolution of the boundary layer thickness δ , as shown in figure 4.

Figure 14 shows the perturbation for $\eta = 0.85$, $\alpha = -0.1$ and $\text{Sc} = 1000$, at $\chi = 5 \times 10^{-5}$ (panel a) and $\chi = 10^{-1}$ (panel b). As osmosis is weak in figure 14(a), the vortices are almost identical to Taylor vortices, and the radial transmembrane flow associated with boundary condition (3.2c) is barely observed. The advection of the concentration boundary layer by the vortices generates patches of solute depletion and accumulation, but these only weakly retro-act on the vortices. As osmosis kicks in in figure 7(b), boundary condition (2.9a) now drives a noticeable extra radial transmembrane flow. This causes the axial wavelength of the vortices to increase. Though five full vortices are observed in figure 14(a), only four are observed along the same axial length in figures 7(b) and 14(b). As the effect of osmosis is further increased between figures 7(b) and 14(b), we also observe a modification of the patches of solute depletion and accumulation,

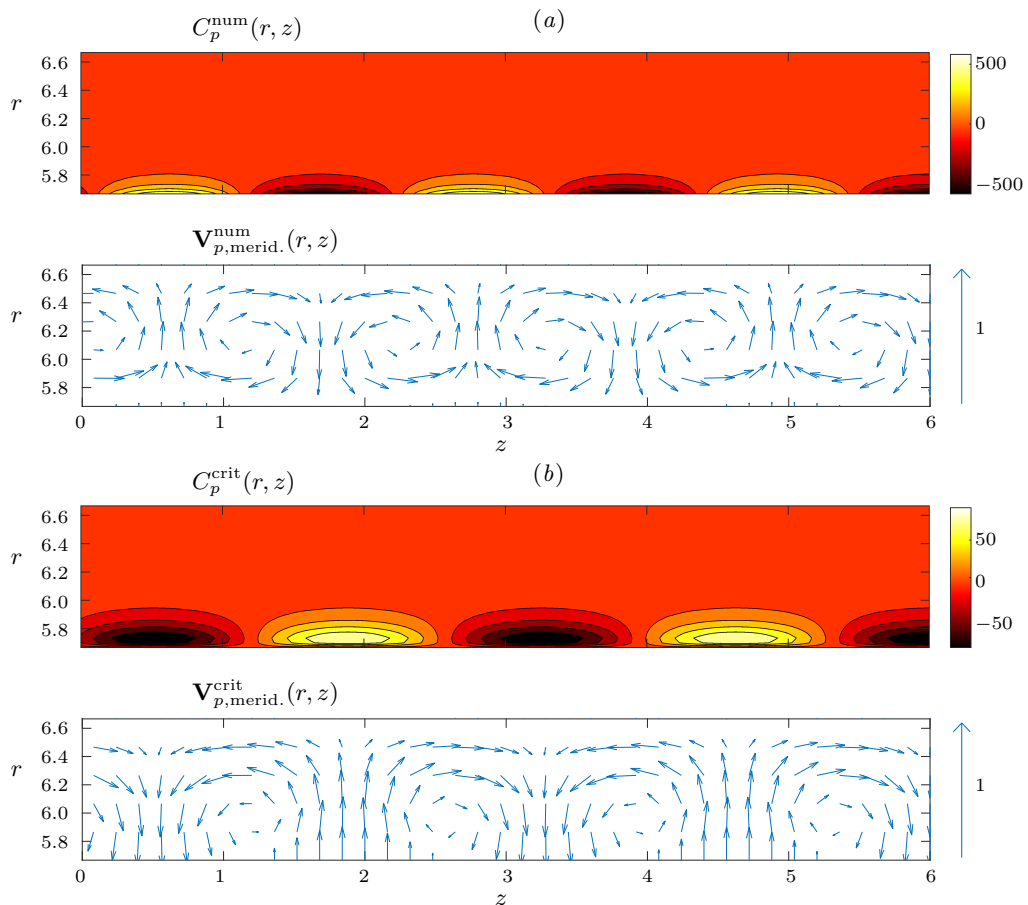


FIGURE 14. Velocity fields of the vortices (U_p, W_p) and concentration perturbation C_p in a meridional plane for $\eta = 0.85$, $\text{Re} = -0.1$, $\text{Sc} = 1000$, and $\chi = 5 \times 10^{-5}$ (a) and $\chi = 10^{-1}$ (b), obtained analytically at critical conditions.

such that the local extrema of these patches detach from the inner cylinder. Together with these detached extrema, the radial transmembrane flow does not further increase. The evolution of the perturbation of concentration and radial velocity fields is further addressed in the next section.

5. How solute rejection favors (or not) the vortices

Here, we further investigate the perturbation flow fields to clarify the mechanism by which the advection of the polarization layer and the related fluctuations of osmotic pressure act on the dynamics of Taylor vortices. This mechanism explains why increasing osmosis first decreases the critical Taylor number, and why this decrease eventually plateaus. In the process, we find an algebraic criterion producing the range of parameters for which osmosis acts on the instability and effectively reduces the critical Taylor number.

For the sake of clarity, we focus on cases of radial inflow $\text{Re} < 0$, with polarization occurring at the inner cylinder. From the numerical results observed in figure 6, we surmised that in the outward (inward) jets, osmosis favors the Taylor vortices by injecting

(extracting) solvent through the inner cylinder. To put this assumption on firmer grounds, we need to identify the mechanism(s) affecting the radial velocity perturbation at the inner cylinder, $u_p(r_1)$. Moreover, we now focus on the axial locations z_{outward} of the radial outward jets where, as in figure 7, the radial velocity perturbation $U_p(r, z_{\text{outward}})$ and concentration perturbation $C_p(r, z_{\text{outward}})$ are positive and identify to their respective radial profiles $u_p(r)$ and $c_p(r)$.

We first recall that in the boundary condition (3.5b) for the radial velocity perturbation, the pressure term is usually weak compared to that due to concentration, such that we can simplify this condition to (4.1), repeated below for convenience

$$u_p(r_i) = \pm \chi c_p(r_i), \quad (5.1)$$

where $r_i = r_1$ or r_2 , and the positive sign is used when $r = r_1$. In addition to the above, $c_p(r)$ also satisfies the scalar transport equation linearized about the base-state. At critical conditions for which the growth rate s vanishes, this equation reads:

$$\underbrace{-\text{Sc} U_b(r) \frac{dc_p}{dr}}_{\textcircled{1}} + \underbrace{\Delta c_p(r)}_{\textcircled{2}} - \underbrace{\text{Sc} u_p(r) \frac{dC_b}{dr}}_{\textcircled{3}} = \text{Sc} s c_p(r) = 0, \quad (5.2)$$

with $\Delta = d_r^2 + \frac{1}{r} d_r - k^2$ and $d_r = d/dr$. Considering (5.2) as the governing equation for $c_p(r)$, term $\textcircled{1}$ represents advection of the scalar by the base flow, term $\textcircled{2}$ represents molecular diffusion and term $\textcircled{3}$ is a source term due to advection of the base-state boundary layer by the Taylor vortices. The concentration perturbation also satisfies the solute rejection condition (3.5c) at both cylinders. Injecting boundary condition (5.1) in the solute rejection condition (3.5c) at the inner cylinder produces the following Robin boundary condition

$$\text{Sc} \left[U_b(r_i) \pm \chi C_b(r_i) \right] c_p(r_i) - \frac{dc_p}{dr}(r_i) = 0, \quad (5.3)$$

where $r_i = r_1$ or r_2 , and the positive sign is used when $r = r_1$. This condition represents the balance between molecular diffusion and advection of c_p by an effective transmembrane flow $U_b(r_1) \pm \chi C_b(r_1)$.

5.1. Coupling in the polarization layer

Figure 15 shows how the increase of the coupling coefficient χ affects the Taylor vortices, the concentration perturbation, and its dynamics. To compare the perturbations $[\mathbf{v}_p(r), c_p(r)]$ at different χ , they are normalized by the maximum of their azimuthal velocity component $v_p(r)$, which is found to be barely affected by osmosis. First, figure 15(a) is a reminder that Ta^{crit} decreases as χ increases, at specific conditions $\text{Sc} = 1000$ and $\text{Re} = -0.1$, in the case of a narrow gap ($\eta = 0.85$). In these conditions, the thickness of the base-state polarization layer is $\delta \approx 0.171$. Figures 15(b) and (c) show how the increase of the coupling coefficient impacts the radial velocity perturbation $u_p(r)$ and concentration perturbation $c_p(r)$, respectively. Figures 15(d) and (e) show how advection terms in the scalar transport equation (5.2), $-\text{Sc} u_p(r) d_r C_b$ and $-\text{Sc} U_b(r) d_r c_p$, respectively, evolve with the coupling coefficient.

In the case of no osmotic pressure, $\chi = 0$ (the dashed horizontal black line in figure 15(a) and black solid curves in figures 15(b) to (e)), the solute has no impact on the centrifugal instabilities, which take the form of the classical Taylor vortices, with no velocity at the inner cylinder $u_p(r_1) = 0$. More specifically, figure 15(b) shows that the radial velocity of these vortices vanishes at the inner cylinder. Due to this boundary condition, the base-state polarization layer and the radial velocity of the vortices barely

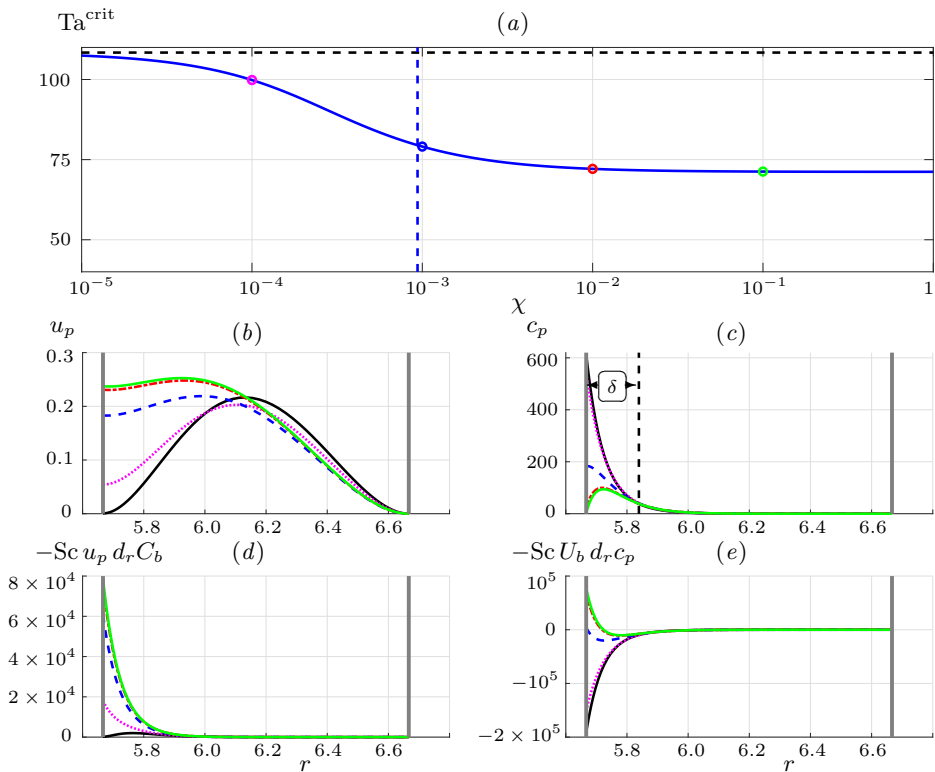


FIGURE 15. (a): Critical Taylor number Ta^{crit} as a function of the coupling coefficient χ in log scale, for $\eta = 0.85$, $\text{Re} = -0.1$ and $\text{Sc} = 1000$. (b): Radial velocity perturbation u_p , (c): Concentration perturbation c_p , the dashed black vertical line bounding the polarization layer, the thickness of which δ is given by (2.15), (d): advection of the bases-state concentration by the radial velocity perturbation (term ③ of equation 5.2) and (e): advection of the concentration perturbation by the base-state radial flow (term ① of equation 5.2), as functions of r , obtained analytically at $\chi = 0$ (solid black curves), 10^{-4} (dotted curves, magenta online), 10^{-3} (dashed curves, blue online), 10^{-2} (dashed-dotted curves, red online) and 10^{-1} (solid light grey curves, green online), the circles in (a) corresponding to the four last cases, whilst the black horizontal dashed line corresponds to the osmosis-free $\chi = 0$ case. The dashed vertical (blue online) line in (a) corresponds to the limit value χ_1 inferred from (5.7).

overlap, such that the source term ③ in equation (5.2), shown as a black curve in figure 15(d), is nearly zero. The transport of the concentration perturbation is thus mostly a balance between its advection by the base-flow $U_b(r)$ and molecular diffusion. For $\chi = 0$, the solute rejection condition (5.3) further reduces to

$$\frac{dc_p}{dr}(r_1) = \text{Sc} U_b(r_1) c_p(r_1). \quad (5.4)$$

Axial diffusion being much weaker than radial diffusion in term ②, the concentration perturbation satisfies the same equation and boundary conditions as the base-state concentration, and $c_p(r)$ is similar, up to a scaling factor, to $C_b(r)$. This can be seen in figure 15(c). Though weak, the positive source term $-Sc u_p d_r C_b$ triggers the coincidence of the radial outward jet with an excess of concentration, or equivalently, a positive radial perturbation velocity $u_p(r)$ (the black curve in figure 15(b)) corresponds to a positive concentration perturbation $c_p(r)$ (the black curve in figure 15(c)).

As χ departs from zero, the radial velocity perturbation no longer vanishes at the

inner cylinder and boundary condition (5.1) implies $u_p(r_1) > 0$. This is illustrated in figure 15(b), where the dotted (magenta online) curve is obtained at $\chi = 10^{-4}$. Osmosis, via this injection of fluid at the inner cylinder, fosters the Taylor vortices and the critical Taylor number decreases accordingly, as reminded in figure 15(a). As the radial velocity perturbation $u_p(r)$ and the base-state concentration $C_b(r)$ now overlap, source term ③ acts in the polarization layer (the dotted, magenta online, curve in figure 15(d)). The concentration perturbation in the polarization layer is also affected by the modification of the solute rejection condition (5.3), where the negative effective transmembrane flow $[U_b(r_1) + \chi C_b(r_1)]$ increases. Outside the polarization layer, the concentration perturbation remains unaffected by osmosis, and similar to the case with $\chi = 0$. Matching the concentration perturbation inside and outside the polarization layer forces $c_p(r_1)$ to decrease and $d_r c_p(r_1)$ to increase as χ increases, as seen in figure 15(c).

For large values of χ , the perturbation tends to a limit solution for which the radial profiles and the critical Taylor number are no longer χ -dependent. This is demonstrated by the asymptotic regime for large values of χ in figure 15(a), and the dash-dotted (red online) and solid light grey (green online) curves in figure 15(b) and (c), obtained at $\chi = 10^{-2}$ and $\chi = 10^{-1}$, respectively. As χ increases, figure 15(b) shows that $u_p(r_1)$ tends to a limit value $u_p^\infty(r_1)$, and figure 15(c) shows that $c_p(r)$ now presents a maximum concentration detached from the inner cylinder, while $c_p(r_1)$ tends to 0. Outside the polarization layer, $c_p(r)$ remains unaffected by osmosis.

To explain this limit regime, first note that at large χ , the solute rejection condition at the inner cylinder (5.3) simplifies to

$$\frac{dc_p}{dr}(r_1) \approx \chi \text{Sc} C_b(r_1) c_p(r_1), \quad (5.5)$$

and $d_r c_p(r_1)$ is now positive. Matching boundary condition (5.5) to the concentration perturbation outside the polarization layer forces $c_p(r)$ to reach its maximum in the polarization layer instead of at the inner cylinder. Furthermore, as χ increases, the solute rejection condition (5.5) forces the concentration perturbation at the inner cylinder $c_p(r_1)$ to decrease and tend to 0, to avoid $u_p(r_1)$ to diverge. The concentration perturbation $c_p(r)$ is now a solution of the transport equation (5.2) with boundary conditions (5.1) and (5.3) rewritten as

$$c_p(r_1) = \frac{1}{\chi} u_p^\infty(r_1) \quad \text{and} \quad \frac{dc_p}{dr}(r_1) = \text{Sc} C_b(r_1) u_p^\infty(r_1), \quad (5.6)$$

respectively. The small value of $c_p(r_1)$ excepted, these solutions are independent of χ . The extra injection of pure solvent at the inner cylinder $u_p(r_1)$ levels off, and no further decrease of Ta^{crit} is observed as χ increases, as seen in figure 15(a).

Figure 15 thus highlights two obvious regimes of coupling between osmosis and Taylor vortices. For small χ , $d_r c_p(r_1)$ is negative, $c_p(r_1)$ is large and $u_p(r_1)$ increases with χ . For large χ , $d_r c_p(r_1)$ is positive, $c_p(r_1)$ is almost zero and $u_p(r_1)$ is independent of χ . The distinction between these two regimes is imposed by the sign of the effective transmembrane velocity $U_b(r_1) + \chi C_b(r_1)$ in the solute rejection boundary condition (5.3). This velocity is negative for small values of χ , and becomes positive when $\chi > \chi_1$, where

$$\chi_1 = \left| \frac{U_b(r_1)}{C_b(r_1)} \right| = \left| \frac{2\text{Re}(1 - \eta)(1 - \eta^{-\text{Re Sc} - 2})}{(\text{Re Sc} + 2)(\eta^{-2} - 1)\eta} \right|. \quad (5.7)$$

This limit value χ_1 is inferred from the base-state alone. It is shown as a dashed vertical (blue online) line at $\chi_1 \approx 9.38 \times 10^{-4}$ in figure 15(a) for $\eta = 0.85$, $\text{Re} = -0.1$ and

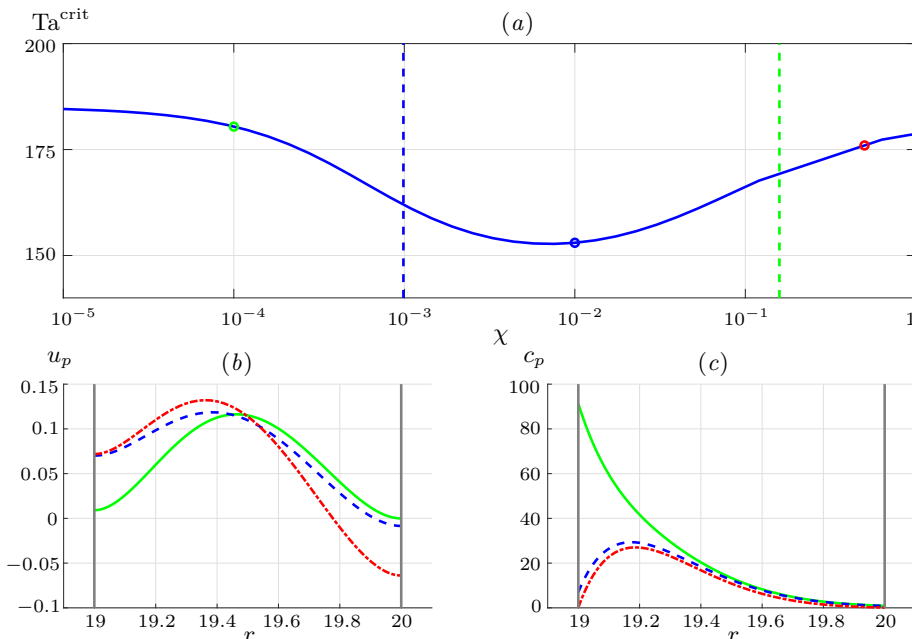


FIGURE 16. (a): Critical Taylor number Ta^{crit} as a function of the coupling coefficient χ , in log scale, for $\eta = 0.95$, $Re = -0.1$ and $Sc = 1000$. (b) Radial velocity perturbation $u_p(r)$ and (c): concentration perturbation $c_p(r)$, obtained analytically at $\chi = 10^{-4}$ (solid curves, green online), 10^{-2} (dashed curves, blue online) and 5×10^{-1} (dashed-dotted curves, red online), the circles in (a) corresponding to these three cases.

$Sc = 1000$. This limit almost corresponds to the dashed, blue online, curves in figures 15(b) to (e) at $\chi = 10^{-3}$. For $\chi < \chi_1$, osmosis favors vortices by injecting pure solvent in the outward jets and extracting pure solvent from the inward jets. In this regime, Ta^{crit} decreases as χ increases. For $\chi > \chi_1$, this mechanism subsides, such that Ta^{crit} plateaus to its limit minimal value. The limit value χ_1 has been added as dark grey (blue online) curves on figures 9 to 11. For sufficiently large Péclet numbers, it indeed coincides, for cases with a radial inflow base-state, to the value of χ beyond which Ta^{crit} is no longer affected by increasing the coupling coefficient.

5.2. Coupling on the depleted side

The solute rejection boundary condition explains another feature of the impact of χ on Ta^{crit} , observed in figures 11(a) and 16(a). For $\eta = 0.95$, $Re = -0.1$ and $Sc = 1000$, Ta^{crit} is found to be a decreasing then increasing function of χ . Concerning the base-state, $\eta = 0.95$ yields a thicker polarization layer $\delta \approx 0.57$ than for $\eta = 0.85$. Accordingly, the solute is less depleted at the outer cylinder for $\eta = 0.95$ than for $\eta = 0.85$. As explained above, in the case of no osmotic pressure, $c_p(r)$ recovers the base-state concentration $C_b(r)$ up to a multiplicative constant and $c_p(r_2)$ noticeably departs from zero for cases with thick polarization layers.

As χ remains limited, the radial velocity perturbation $u_p(r)$ and concentration perturbation $c_p(r)$ and their evolution with χ at $\eta = 0.95$ are similar to the case $\eta = 0.85$, and governed by osmosis and the advection of the polarization layer at the inner cylinder. This is demonstrated in figures 16(b) and (c), where the solid (green online) curves are obtained at $\chi = 10^{-4}$ and dashed (blue online) curves at $\chi = 10^{-2}$. As χ is further

increased, the radial velocity perturbation at the outer cylinder, $u_p(r_2)$, substantially departs from 0, to be negative. This is illustrated in figure 16(b) where the dash-dotted (red online) curve is obtained at $\chi = 5 \times 10^{-1}$. This counter-flow acts against the outward jet and explains the increase of the critical Taylor number, as reminded in figure 16(a). This counter-flow is induced by the boundary condition for $u_p(r)$ at the outer cylinder

$$u_p(r_2) = -\chi c_p(r_2). \quad (5.8)$$

Moreover, as the source term ③ in the transport equation (5.2) vanishes outside the polarization layer, $d_r c_p(r_2)$ must be independent of χ . In the solute rejection condition at the outer cylinder

$$\text{Sc} \left[U_b(r_2) - \chi C_b(r_2) \right] c_p(r_2) - \frac{dc_p}{dr}(r_2) = 0, \quad (5.9)$$

the (negative) effective transmembrane velocity $U_b(r_2) - \chi C_b(r_2)$ decreases with χ , and forces $c_p(r_2)$ to tend to zero as χ increases.

For large values of χ , the solute rejection condition further reduces to

$$\frac{dc_p}{dr}(r_2) \approx -\chi \text{Sc} C_b(r_2) c_p(r_2), \quad (5.10)$$

and forces $u_p(r_2) = -\chi c_p(r_2)$ to tend to a negative limit value $u_p^\infty(r_2)$. The limit regime at the outer cylinder occurs as χ exceeds

$$\chi_2 = \left| \frac{U_b(r_2)}{C_b(r_2)} \right| = \left| \frac{2\text{Re}(1-\eta)(1-\eta^{\text{Re Sc}+2})}{(\text{Re Sc}+2)(\eta^2-1)} \right|, \quad (5.11)$$

and $-\chi C_b(r_2)$ becomes dominant over $U_b(r_2)$ in boundary condition (5.9). The limit value (5.11) has been added as light grey (green online) curves in figures 9 to 11. It roughly coincides, for cases with a radial inflow bases-state, to the value of χ beyond which the decrease of Ta^{crit} due to osmosis at the inner cylinder is no longer observed.

6. Range of parameters where osmosis favors the vortices

The parametric study in §4.2 has shown that the critical conditions Ta^{crit} of the centrifugal instabilities eventually depend on three parameters: the Péclet number $\text{Pe} = \text{Re Sc}$, the velocity-concentration coupling coefficient renormalized by the Schmidt number χSc , and the radius ratio η . More specifically, combining the limit values (5.7) and (5.11) found in §5, osmosis is found to impact the centrifugal instabilities and decreases Ta^{crit} for χSc in the range

$$\underbrace{\frac{2\text{Pe}(1-\eta^{-\text{Pe}-2})\eta}{(\text{Pe}+2)(1+\eta)}}_{\chi_1 \text{Sc}} < \chi \text{Sc} < \underbrace{\frac{2\text{Pe}(\eta^{\text{Pe}+2}-1)}{(\text{Pe}+2)(1+\eta)}}_{\chi_2 \text{Sc}} \quad \text{for } \text{Pe} < 0, \quad (6.1)$$

in terms of (negative) Péclet number, for radial inflow base-states, and η . For cases with radial outflow base-states, as in figure 9(b), the inner and outer cylinders exchange their roles. For $\chi \text{Sc} > \text{Sc} U_b(r_2)/C_b(r_2)$, osmotic pressure at the outer cylinder no longer further favors the outward and inward jets of the vortices and Ta^{crit} tends to its limit minimal value. For $\chi \text{Sc} > \text{Sc} U_b(r_1)/C_b(r_1)$, osmotic pressure at the inner cylinder hampers the outward and inward jets of the vortices, and Ta^{crit} increases with χ . Osmosis

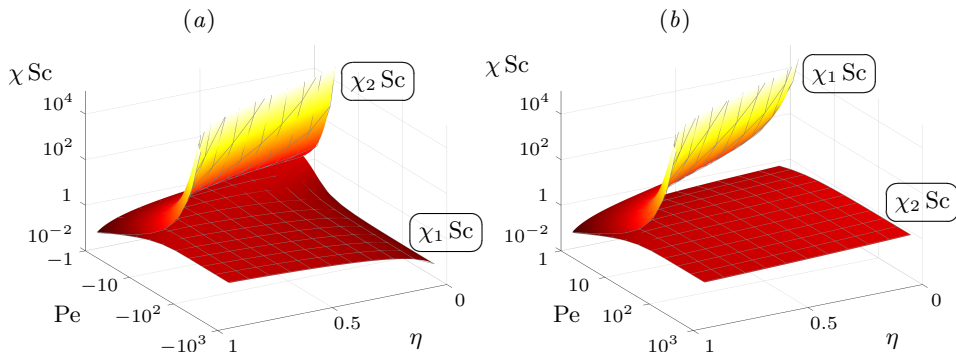


FIGURE 17. Limit values $\chi_1 Sc$ and $\chi_2 Sc$, bounding the χSc range where osmosis lessens the critical Taylor number, as functions of η and Pe , shown for (a): radial inflows ($Pe < 0$) and (b): radial outflows ($Pe > 0$).

consequently decreases Ta^{crit} for χSc in the range

$$\underbrace{\frac{2Pe(1-\eta^{\text{Pe}+2})}{(Pe+2)(1+\eta)}}_{\chi_2 Sc} < \chi Sc < \underbrace{\frac{2Pe(\eta^{-\text{Pe}-2}-1)\eta}{(Pe+2)(1+\eta)}}_{\chi_1 Sc} \quad \text{for } Pe > 0, \quad (6.2)$$

in terms of (positive) Péclet numbers and η .

Figure 17 shows χSc -ranges (6.1) (panel *a*) and (6.2) (panel *b*), between the two surfaces $\chi_1 Sc$ and $\chi_2 Sc$ as functions of η and Pe . In configurations with $(Pe, \eta, \chi Sc)$ between the two surfaces, instabilities are affected by osmosis. The larger this χSc -range between the two surfaces is, the more the enhancement of the vortices by osmosis accommodates variations of χ due, for instance, to variations of the mean concentration C_0 . Figure 17 shows that a higher Péclet number enlarges the χSc -range. Figure 17 also shows that a narrow gap (large η) presents a limited χSc -range compared to a wide gap (small η). For osmosis to enhance the Taylor vortices over a substantial χSc -range, a higher Péclet number must therefore be reached in a narrow gap than in a wide gap.

The dependence of critical conditions with Pe , χSc and η is eventually recast into a simpler but cruder form. Within the χSc -ranges (6.1) and (6.2) as shown in figure 17, the critical Taylor number Ta^{crit} is approximated by its asymptotic value for large χSc and Pe , $Ta_{\text{min}}^{\text{crit}}$, as defined in §4.2. Outside these ranges, Ta^{crit} is approximated by the critical Taylor number for Taylor vortices in pure solvent $Ta_{\text{pure}}^{\text{crit}}$. Both $Ta_{\text{min}}^{\text{crit}}$ and $Ta_{\text{pure}}^{\text{crit}}$ are functions of the radius ratio η only. Figure 18 shows $Ta_{\text{pure}}^{\text{crit}}$ (the dashed curves in panels *a* and *b*) and $Ta_{\text{min}}^{\text{crit}}$ (the solid curves in panels *a* and *b*), as functions of η , in the case of a radial inflow (panel *a*) and radial outflow (panel *b*). Figures 18(*c*) and (*d*) show the corresponding ratio ϵ as defined in (4.2). As figure 11 showed that Ta^{crit} reached a minimum at $Sc = 2000$ and $\chi = 0.023$ for $\eta = 0.95$ and $Re = -0.1$, we approximate the asymptotic critical Taylor number as $Ta_{\text{min}}^{\text{crit}} \approx Ta_{\text{min}}^{\text{crit}}|_{|Pe|=200, \chi Sc=46}$. For both in- and outflows, variations of $Ta_{\text{min}}^{\text{crit}}$ are found to mostly follow those of $Ta_{\text{pure}}^{\text{crit}}$. The absolute difference $Ta_{\text{pure}}^{\text{crit}} - Ta_{\text{min}}^{\text{crit}}$ is fairly constant and larger for inflows than for outflows, due to the fact that a radial inflow develops a steeper concentration boundary layer at the inner cylinder than the corresponding radial outflow does at the outer cylinder. In terms of relative difference, the ratio ϵ is thus substantially larger for the inflow than for the outflow. Moreover, a maximum value $\epsilon_{\text{max}} = 0.271$ is reached for a narrow gap

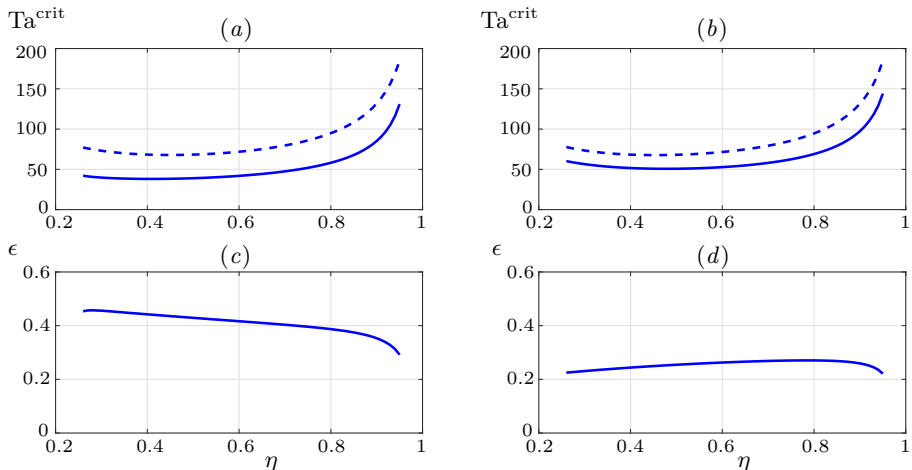


FIGURE 18. Asymptotic critical Taylor number Ta_{\min}^{crit} approximated by the critical Taylor number $Ta_{\min}^{\text{crit}}|_{|Pe|=200, \chi Sc=46}$ at Péclet number $|Pe| = 200$ and coupling coefficient $\chi Sc = 46$ (solid curves) and critical Taylor number for pure solvent $Ta_{\text{pure}}^{\text{crit}}$ (dashed curves), as functions of the radius ratio η , for radial outflows (a) and inflows (b). Bottom row: corresponding ratio $\epsilon = 1 - Ta_{\min}^{\text{crit}}/Ta_{\text{pure}}^{\text{crit}}$.

at $\eta = 0.78$ in the cases of outflows. In the cases of inflows, ϵ is found to increase as η decreases over almost the whole covered range $0.25 \geq \eta \geq 0.95$, and a maximum $\epsilon_{\max} = 0.457$ is reached for a wide gap at $\eta = 0.265$.

7. Conclusions and outlook

This study has shown by linear stability analyses and DNS that the coupling of Taylor vortices with the osmotic pressure associated with concentration polarization near a semi-permeable membrane tends to reduce the critical Taylor number above which vortices appear by up to 40%. The reduction of Ta^{crit} matches the increase of the effective size of the vortices and they are both outcomes of the non-zero boundary condition for the perturbation of transmembrane velocity (3.2a). By injections and extractions of fluid coinciding with outward and inward jets of the vortices, respectively in the case of a mean radial inflow, this condition promotes the hydrodynamic instabilities. This condition also allows vortices to “penetrate” the permeable boundary (as seen in figure 14) and increase their effective radial extension. To limit their viscous dissipation, the vortices also increase their axial extension, and the decrease of Ta^{crit} observed in figure 11 thus corresponds to the increase of λ^{crit} in figure 12. These instabilities remain driven by centrifugal forces, but are fostered by osmotic pressure. It has never been found so far that osmosis alone could sustain the growth of instabilities.

Besides the Taylor number, this mechanism is eventually governed by three physical parameters: the radial Péclet number $Pe = Re Sc = U|_{r=r_1} r_1/\mathcal{D}$ governing the steepness of concentration polarization, a coupling coefficient $\chi Sc = KRTdC_0/\mathcal{D}$ scaling the retroaction of the osmotic pressure on the transmembrane velocity with respect to the damping effects of molecular diffusion, and the radius ratio $\eta = r_1/r_2$. Based on these three physical parameters, the reduction of Ta^{crit} is observed in a χSc -range, given by equations (6.1–6.2), and function of Pe and η . Within this range, Ta^{crit} plateaus at a

limit value Ta_{\min}^{crit} , shown in figure 18 as a function of η . At this point, it remains unclear, though, if Ta_{\min}^{crit} is truly independent of Pe or a slowly varying function of this parameter.

Despite the Reynolds number $Re = U|_{r_1} r_1 / \nu$ being introduced as one of the physical parameters to conform with previous studies, the imposed radial flow remains limited in this study, in consistency with the weak transmembrane velocities observed in real RO ($|Re| \sim 10^{-2} - 10^{-1}$). In itself, this radial flow has a very limited effect on the hydrodynamic instabilities. Larger radial Reynolds numbers, though, are known to directly alter these instabilities (see Martinand *et al.* 2017) and addressing set-ups with larger radial through-flow should reconsider the Reynolds number as a relevant parameter. The velocity-pressure coupling coefficient $\sigma = K\rho\nu/d$ has also been found to be of limited impact for typical RO set-ups where it is very weak ($\sigma \sim 10^{-12} - 10^{-13}$). Beyond such cases with very weak permeance K , the effect of σ on the hydrodynamic instabilities has been found, for $\eta = 0.85$, to be negligible up to $\sigma \sim 10^{-3}$, a value hardly reached in any filtration set-up.

The capacity of the hydrodynamic instabilities to reduce the osmotic counter-pressure and improve the performance of filtration devices is the key point of dynamic filtration, and assessing this capacity is the next step of our work. More precisely, dynamic filtration assumes that for a given mean transmembrane flow, hydrodynamic instabilities abate the mean concentration boundary layer, thus reducing the related osmotic pressure and power required to drive solvent across the membrane. The question can be equivalently reformulated to determine if, at given working pressure ΔP , the mean transmembrane flow increases in the presence of instabilities. Analytically, this question cannot be addressed by linear stability analysis, as the sinusoidal axial variations of the transmembrane flow perturbation lead to a zero mean value for this extra transmembrane flow. The non-linear retroaction of the instabilities on the base-state must therefore be considered. Our set-up and approach offers two ways to address the question. First, DNS have been found to work well and can be used to explore the non-linear dynamics of the flow, including the extra transmembrane flow. A closer look at figures 6(a) and (b) already reveals some aspects of this non-linearity, even though the DNS at $Ta = 90$ only slightly departs from the critical conditions ($Ta^{\text{crit}} = 79.1$). The radial component of the velocity U^{num} and the concentration C^{num} exhibit an unbalance between the crests and troughs, the latter being more pronounced. Moreover, averaging these fields along the axial direction shows that the presence of the vortices decreases the mean concentration at the membrane and increases (in absolute value) the mean radial fluid flux across the cell accordingly, by $\sim 50\%$ with respect to the corresponding base state (the dark grey, blue online, frames). This test case hence supports the hypothesis that vortices improve filtration. Next, a weakly non-linear stability analysis, by including a modification of the mean radial flow, could also help explain how transmembrane flow is affected by the instabilities. A parametric study based on this weakly non-linear stability analysis could hence provide a framework for optimizing the configuration of filtration devices. We are currently working along both lines.

Extending the study of the coupling between concentration polarization, osmotic pressure and hydrodynamic instabilities to more realistic geometries is another outlook. First, a configuration in which a net flux of solvent is extracted requires the addition of a mean axial flow and complicates the stability analysis. The development of global modes of instability in such an open system has been addressed for pure solvent flows in Tilton & Martinand (2018). Whereas no direct extension of this theoretical analysis to cases with solutes and osmosis has been found so far, due to a lack of analytical base-state, we are currently working to adapt the DNS to take into account a mean axial flow. Next, the coupling between osmosis and vortices described here does not seem specific to

centrifugal instabilities, and other types of flows and instabilities, such as Dean vortices, Görtler vortices, boundary layers, and Tollmien–Schlichting waves, could be addressed, as they are more relevant to industrial filtration devices.

The base-state computed in this Taylor–Couette set-up shows that the maximum concentration in the boundary layer grows with the Péclet number Pe , and rapidly experiences an increase over several orders of magnitude (see figure 4). Moreover, on top of the bases-state, hydrodynamic instabilities generate supplemental peaks of concentration (see figure 6). This study has solely focused on the effect of concentration polarization on osmotic pressure. Nevertheless, concentration polarization causes several other phenomena. Changes in the base state and in the critical conditions of the instabilities are induced by the concentration-related variations of the physical properties of the solution (see Nayar *et al.* 2018, for seawater). Doubling the solubility from 35 g/kg of typical seawater to 70 g/kg increases its dynamic viscosity μ by $\sim 8\%$ and its density ρ by $\sim 3\%$ so the Taylor number Ta decreases by $\sim 5\%$. Simultaneously, assuming the Stokes–Einstein relation $\mathcal{D}\mu = \text{cste}$, the molecular diffusivity \mathcal{D} decreases by $\sim 8\%$ so both the Péclet number Pe and χSc increase by $\sim 8\%$. Furthermore, the increase of the concentration above the maximum solubility induces the precipitation of the solute, which can form a gel layer changing the rheology of the fluid. In seawater, whereas sodium chloride does not precipitate for total solubilities up to 350 g/kg, magnesium hydroxide is already in the form of a suspension at 35 g/kg. Moreover, high concentrations also impact the properties of the membrane by adsorption of the solute or clogging by precipitates. This generally decreases the membrane permeance K and rejection rate, which has been assumed to be 1 in this study.

Sorting out the relative importance of all these mechanisms would require careful experiments. By its precise controls of the concentration polarization and hydrodynamic instabilities, the present Taylor–Couette set-up could prove useful, albeit requiring extra cares to handle the radial flow and large operating pressures, together with the rotating cylindrical, usually opaque, membranes.

P. Haldenwang and C. Lemaitre are gratefully acknowledged for fruitful discussions and helpful comments.

This work was supported by the Thomas Jefferson Fund of the Embassy of France in the United States and the FACE foundation (grant TJF18-131) and by the National Science Foundation (N.T., CAREER Award 1752531). Declaration of Interest. The authors report no conflict of interest.

Appendix A. Base state

Solving equations (2.7) with boundary conditions (2.9) produces the following steady, axially and azimuthally invariant, base-flow [$\mathbf{V}_b(r)$, $P_b(r)$, $C_b(r)$]:

$$W_b(r) = 0 \quad \text{and} \quad U_b(r) = \frac{\text{Re}}{r}, \quad (\text{A } 1)$$

$$V_b(r) = \begin{cases} \frac{\text{Ta } r_1}{r} \frac{1 - (r/r_2)^{\text{Re}+2}}{1 - \eta^{\text{Re}+2}} & \text{for } \text{Re} \neq -2 \\ \frac{\text{Ta } r_1}{r} \frac{\log(r/r_2)}{\log(\eta)} & \text{for } \text{Re} = -2, \end{cases} \quad (\text{A } 2)$$

- AHMAD, A. L. & LAU, K. K. 2006 Impact of different spacer filaments geometries on 2D unsteady hydrodynamics on concentration polarization in spiral wound membrane channel. *J. Membr. Sci.* **286**, 77–92.
- AKONUR, A. & LUEPTOW, R. M. 2002 Chaotic mixing and transport in wavy Taylor–Couette flow. *Physica D* **167**, 183–196.
- ALJISHI, M. F., RUO, A. C., PARK, J. H., NASSER, B., KIM, W. S. & JOO, Y. L. 2013 Effect of flow structure at the onset of instability on barium sulfate precipitation in Taylor–Couette crystallizers. *J. Cryst. Growth* **373**, 20–31.
- ANDERECK, C. D., LIU, S. S. & SWINNEY, H. L. 1986 Flow regimes in a circular Couette system with independently rotating cylinders. *J. Fluid Mech.* **164**, 155–183.
- BAHL, S. K. 1970 Stability of viscous flow between two concentric rotating porous cylinders. *Def. Sci. J.* **20**, 89–95.
- BEAUDOIN, G. & JAFFRIN, M. Y. 1989 Plasma filtration in Couette flow membrane devices. *Artif. Organs* **13** (1), 43–51.
- BEAVERS, G. S. & JOSEPH, D. D. 1967 Boundary conditions at a naturally permeable wall. *J. Fluid Mech.* **30**, 197–207.
- BELFORT, G., MIKULASEK, P., PIMBLEY, J. M. & CHUNG, K. Y. 1993*a* Diagnosis of membrane fouling using a rotating annular filter. 2. Dilute particule suspension of known particule size. *J. Membr. Sci.* **77** (1), 23–39.
- BELFORT, G., PIMBLEY, J. M., GREINER, A. & CHUNG, K. Y. 1993*b* Diagnosis of membrane fouling using a rotating annular filter. 1. Cell culture media. *J. Membr. Sci.* **77** (1), 1–22.
- BERNALES, B., HALDENWANG, P., GUICHARDON, P. & IBASETA, N. 2017 Prandtl model for concentration polarization and osmotic counter-effects in a 2-D membrane channel. *Desalination* **404**, 341–359.
- BILSON, M. & BREMHORST, K. 2007 Direct numerical simulation of turbulent Taylor–Couette flow. *J. Fluid Mech.* **579**, 227–270.
- COLE, J. A. 1976 Taylor vortex instability and annulus-length effects. *J. Fluid Mech.* **75**, 1–15.
- COLES, D. 1965 Transition in circular Couette flow. *J. Fluid Mech.* **21**, 385–425.
- DAVEY, A., DIPRIMA, R. C. & STUART, J. T. 1968 On the instability of Taylor vortices. *J. Fluid Mech.* **31**, 17–52.
- GHAFFOUR, N., MISSIMER, T. M. & AMY, G. L. 2013 Technical review and evaluation of the economics of water desalination: Current and future challenges for better water supply sustainability. *Desalination* **309**, 197–207.
- GIORDANO, R. L. C., GIORDANO, R. C. & COONEY, C. L. 2000*a* Performance of a continuous Taylor–Couette–Poiseuille vortex flow enzymic reactor with suspended particles. *Process Biochem.* **35**, 1093–1101.
- GIORDANO, R. L. C., GIORDANO, R. C., PRAZERES, D. M. F. & COONEY, C. L. 2000*b* Analysis of a Taylor–Poiseuille vortex flow reactor — II: reactor modeling and performance assessment using glucose-fructose isomerization as test reaction. *Chem. Eng. Sci.* **55**, 3611–3626.
- HAIDARI, A. H., HEIJMAN, S. G. J. & VAN DER MEER, W. G. J. 2016 Vizualization of hydraulic conditions inside the feed channel of Reverse Osmosis: A practical comparison of velocity between empty and spacer-filled channel. *Water Res.* **106**, 232–241.
- HAIDARI, A. H., HEIJMAN, S. G. J. & VAN DER MEER, W. G. J. 2018*a* Effect of spacer configuration on hydraulic conditions using PIV. *Sep. Purif. Technol.* **199**, 9–19.
- HAIDARI, A. H., HEIJMAN, S. G. J. & VAN DER MEER, W. G. J. 2018*b* Optimal design of spacers in reverse osmosis. *Sep. Purif. Technol.* **192**, 441–456.
- HALDENWANG, P., GUICHARDON, P., CHIAVASSA, G. & IBASETA, N. 2010 Exact solution to mass transfer in berman flow: Application to concentration polarization combined with osmosis in crossflow membrane filtration. *Int. J. Heat and Mass Trans.* **53**, 3898–3904.
- HALLSTRÖM, B. & LOPEZ-LEIVA, M. 1978 Description of a rotating ultrafiltration module. *Desalination* **24** (1–3), 273–279.
- KOSHMIEDER, E. L. 1993 *Bénard cells and Taylor vortices*. Cambridge University Press.
- KRONER, K. H. & NISSINEN, V. 1988 Dynamic filtration of microbial suspension using an axially rotating filter. *J. Membr. Sci.* **36**, 85–100.
- LOPES, G. H., BERNALES, B., IBASETA, N., GUICHARDON, P. & HALDENWANG, P. 2012 Prediction of permeate flux and rejection rate in ro and nf membrane processes: Numerical

- modelling of hydrodynamics and mass transfer coupling. *Procedia Engineering* **44**, 1934–1936.
- LOU, J., JOHNSTON, J., CATH, T. Y., MARTINAND, D. & TILTON, N. 2020 Computational fluid dynamics simulations of steady and unsteady mixing in spacer-filled direct contact membrane distillation channels. *submitted to J. Membr. Sci.* .
- LOU, J., VANNESTE, J., DECALUWE, S. C., CATH, T. Y. & TILTON, N. 2019 Computational fluid dynamics simulations of polarization phenomena in direct contact membrane distillation. *J. Membr. Sci.* **591**, 117150.
- LUEPTOW, R. M. & HAJILOO, A. 1995 Flow in a rotating membrane plasma separator. *Am. Soc. Artif. Int. Organs* **41** (2), 182–188.
- LYSTER, E., AU, J., RALLO, R., GIRALT, F. & COHEN, Y. 2009 Coupled 3-D hydrodynamics and mass transfer analysis of mineral scaling-induced flux decline in a laboratory plate-and-frame reverse osmosis membrane module. *J. Membr. Sci.* **339**, 39–48.
- MANSOURI, J., HARRISSON, S. & CHEN, V. 2010 Strategies for controlling biofouling in membrane filtration systems: challenges and opportunities. *J. Mater. Chem.* **20**, 4567–4586.
- MARCUS, P. S. 1984 Simulation of Taylor–Couette flow. Part 2. Numerical results for wavy vortex flow with one travelling wave. *J. Fluid Mech.* **146**, 65–113.
- MARGARITIS, A. & WILKE, C. R. 1978 The Rotorfermentor. I. Description of the apparatus power requirements, and mass transfer characteristics. *Biotech. Bioeng.* **20** (5), 709–726.
- MARTINAND, D., SERRE, E. & LUEPTOW, R. M. 2009 Absolute and convective instability of cylindrical Couette flow with axial and radial flows. *Phys. Fluids* **21**, 104102.
- MARTINAND, D., SERRE, E. & LUEPTOW, R. M. 2017 Weakly nonlinear analysis of cylindrical Couette flow with axial and radial flows. *J. Fluid Mech.* **824**, 438–476.
- MIN, K. & LUEPTOW, R. M. 1994 Hydrodynamic stability of viscous flow between rotating porous cylinders with radial flow. *Phys. Fluids* **6** (1), 144–151.
- MIYASHITA, T. & SENNA, M. 1993 Development of Taylor Vortices in a concentrated suspension comprising monodispersed microspheres. *J. Colloid Interface Sci.* **155**, 290–296.
- NAYAR, K. G., SHARQAWY, M. H. & LIENHARD, J. H. 2018 Seawater Thermophysical Properties Library. *Tech. Rep.*. MIT, <http://web.mit.edu/seawater> (last access 2021-05-17).
- NEMRI, M., CLIMENT, E., CHARTON, S., LANOË, J-Y. & ODE, D. 2013 Experimental and numerical investigation on mixing and axial dispersion in Taylor–Couette flow patterns. *Chem. Eng. Res. Des.* **91**, 2346–2354.
- OHASHI, K., TASHIRO, K., KUSHIYA, F., MATSUMOTO, T., YOSHIDA, S., ENDO, M., HORIO, T., OSAWA, K. & SAKAI, K. 1988 Rotation-induced Taylor vortex enhances filtrate flux in plasma separation. *Trans. Am. Soc. Artif. Intern. Organs J.* **34** (3), 300–307.
- OSTILLA-MONICO, R., VAN DER POËL, E. P., VERZICCO, R., GROSSMANN, S. & LOHSE, D. 2014 Exploring the phase diagram of fully turbulent Taylor–Couette flow. *J. Fluid Mech.* **761**, 1–26.
- RASPO, I., HUGHES, S., SERRE, E., RANDRIAMAMPINANINA, A. & BONTOUX, P. 2002 A spectral projection method for the simulation of complex three-dimensional rotating flows. *Comp. Fluids* **31** (4–7), 745–767.
- SABLANI, S. S., GOOSEN, M. F. A., AL-BELUSH, R. & WILF, M. 2001 Concentration polarization in ultrafiltration and reverse osmosis: a critical review. *Desalination* **141**, 269–289.
- SCHWILLE, J. A., MITRA, D. & LUEPTOW, R. M. 2002 Design parameters for rotating filtration. *J. Membr. Sci.* **204** (1–2), 53–65.
- SERRE, E., SPRAGUE, M. A. & LUEPTOW, R. M. 2008 Stability of Taylor–Couette flow in a finite-length cavity with radial through-flow. *Phys. Fluids* **20** (3), 034106.
- TAYLOR, G. I. 1923 Stability of a viscous liquid contained between two rotating cylinders. *Phil. Trans. R. Soc. A* **223**, 289–343.
- TILTON, N. & MARTINAND, D. 2018 Taylor–Couette–Poiseuille flow with a weakly permeable inner cylinder: absolute instabilities and selection of global modes. *J. Fluid Mech.* **849**, 741–776.
- TILTON, N., MARTINAND, D., SERRE, E. & LUEPTOW, R. 2012 Incorporating Darcy’s law for

- pure solvent flow through porous tubes : asymptotic solution and numerical simulation. *AIChE J.* **58**, 2030–2044.
- TILTON, N., MARTINAND, D., SERRE, E. & LUEPTOW, R. M. 2010 Pressure-driven radial flow in a Taylor–Couette cell. *J. Fluid Mech.* **660**, 527–537.
- TILTON, N., SERRE, E., MARTINAND, D. & LUEPTOW, R. M. 2014 A 3D pseudospectral algorithm for fluid flows with permeable walls. Application to filtration. *Comput. Fluids* **93**, 129–145.
- VANEL, J. M., PEYRET, R. & BONTOUX, P. 1986 A pseudospectral solution of vorticity streamfunction equations using the influence matrix technique. In *Numerical Methods for Fluid Dynamics II* (ed. K. W. Morton & M. J. Baines), pp. 463–475. Oxford: Clarendon Press.
- VAN WAGNER, E. M., SAGLE, A. C., SHARMA, M. M. & FREEMAN, B. D. 2009 Effect of crossflow testing conditions, including feed pH and continuous feed filtration, on commercial reverse osmosis membrane performance. *J. Membr. Sci.* **345**, 97–109.
- WANG, J., DLAMINI, D. S., MISHRA, A. K., PENDERGAST, M. T. M., WONG, M. C. Y., MAMBA, B. B., FREGER, V., VERLIEFDE, A. R. D. & HOEK, E. M. V. 2014 A critical review of transport through osmotic membranes. *J. Membr. Sci.* **454**, 516–537.